AGE, PETROGENESIS AND TECTONIC IMPLICATIONS OF THE LATE PERMIAN PERALUMINOUS AND METALUMINOUS MAGMATIC ROCKS IN THE MIDDLE GOBI VOLCANOPLUTONIC BELT, MONGOLIA

Ariuntsetseg Ganbat [1,2,*] **ariun.0602@gmail.com**

Tatsuki Tsujimori [1,3] **tatsukix@tohoku.ac.jp**

Laicheng Miao [4] **miaolc@mail.iggcas.ac.cn**

Inna Safonova [5,6] **inna03-64@mail.ru**

Daniel Pastor-Galán [1,3,7] **dpastorgalan@gmail.com**

Chimedtseren Anaad [2,9] **chimedtserena@yahoo.com**

Shogo Aoki [10,11] **s-aoki@gipc.akita-u.ac.jp**

Kazumasa Aoki [11] **kazumasa@das.ous.ac.jp**

[1] Department of Earth Science, Graduate School of Science, Tohoku University, Aoba, Sendai 980-8578, Japan
[2] Geoscience Center, Mongolian University of Science and Technology, Ulaanbaatar 120646, Mongolia
[3] Center for Northeast Asian Studies, Tohoku University, Aoba, Sendai 980-8576, Japan
[4] Institute of Geology and Geophysics, Chinese Academy of Sciences, Beijing 100029, China
[5] Novosibirsk State University, Pirogova St. 1, Novosibirsk, 630090, Russia
[6] Sobolev Institute of Geology and Mineralogy, SB RAS, Koptyuga ave. 3, Novosibirsk, 630090, Russia
[7] Frontier Research Institute for Interdisciplinary Sciences, Tohoku University, Aoba, Sendai 980- 0845, Japan
[8] Mongolian University of Science and Technology, Ulaanbaatar 120646, Mongolia
[9] Natural History Museum of Mongolia, Ulaanbaatar, 120646, Mongolia
[10] Graduate School of International Resource Sciences, Akita University, Akita 010-8502, Japan
[11] Center for Fundamental Education, Okayama University of Science, Okayama 700-0005, Japan

---

This Manuscript has been submitted for publication in Island Arc in September 2021. Please note that despite having undergone peer-review, the manuscript has not been formally accepted yet for publication and, therefore, it may be subject to some changes. Subsequent versions of the manuscript may include slightly different content. If accepted the final version of the manuscript will be available through the “PEER REVIEW PUBLICATION DOI” link.

Abstract

The Mongol–Okhotsk Belt, the youngest segment of the Central Asian Orogenic Belt, formed by the evolution and closure of the Mongol–Okhotsk Ocean. The oceanic closure formed two volcanoplutonic belts: Selenge Belt in the north and Middle Gobi Belt in the south (in present day coordinates). However, the origin and tectonic evolution of the Mongol–Okhotsk Belt in general, the origin and formation age of the Middle Gobi Belt in particular, remain enigmatic. To better understand the history of the magmatic activity in the Middle Gobi Belt, we conducted geochemical, U–Pb geochronological, zircon Hf, whole-rock Nd isotopic analyses of volcanic and plutonic rocks of the Mandalgovi suite, the major component of the Middle Gobi Belt. Our results show that the Mandalgovi suite consists of (i) 265 ± 2 Ma biotite-granite; (ii) 250 ± 3 Ma hornblende-granitoids; (iii) their volcanic equivalents of both: and (iv) gabbro-diorites. The geochemical compositions indicate that their precursor magmas were derived from crustal source. The protoliths of the biotite and hornblende-granitoids were metagraywacke and metabasalt, respectively. They are characterized by positive whole-rock $\varepsilon_{Nd}(t)$ and zircon $\varepsilon_{Hf}(t)$ values, indicating the molten protoliths were juvenile crust. The biotite-granites formed by remelting of fore-arc sediments by ridge subduction and later hornblende-granites were emplaced at an intra-oceanic arc by the subduction of the Mongol–Okhotsk Ocean. We conclude that the magmatic rocks of the Middle Gobi formed in an active continental margin and/or intra-oceanic arc setting.

1. Introduction

The growth of the continental crust has represented one of the most exciting debates in the Earth Sciences for at least the last three decades (e.g., Taylor and McLennan, 1985; Jahn et al., 2000; Kemp et al., 2006; Kröner et al., 2014, 2017; Rino et al., 2008; Belousova et al., 2010; Ganbat et al., 2021a). Pioneering research pointed out that the formation of continental crust was episodical and most of its volume formed in the Precambrian (e.g., Armstrong, 1981). However, more recent studies suggest that significant continental growth took place during the Phanerozoic (Jahn, 2004; Hawkesworth et al., 2010; Safonova, 2017; Rosembaum, 2018). Understanding the continental growth during the Phanerozoic can provide crucial knowledge on the mechanisms of magmatic differentiation from the mantle to the crust, as well as important perceptions about the compositions and evolution of the continental crust.

The Central Asian Orogenic Belt (CAOB) is the world largest Pacific-type accretionary orogeny. It is located between Siberia, Kazakhstan, Tarim, and North China, and has a long history from the Neoproterozoic to the late Paleozoic of continuous amalgamation of multiple microcontinents, island arcs, oceanic plateaus, seamounts, ophiolites, and accretionary complexes after suturing at least two oceans (Paleo-Asian and Mongol–Okhotsk Oceans) and possibly several seaways and back-arcs (e.g., Zonenshain et al., 1990; Dobretsov et al., 1995; Buslov et al., 2001; Xiao et al., 2003; Windley et al., 2007; Safonova et al., 2011, Safonova, 2017; Wilhem et al., 2012; Yakubchuk, 2017). The CAOB is also the locus of rapid and extensive juvenile granitic formation during the Phanerozoic, but the petrogenesis, geodynamic and relationships with CAOB's crustal growth are controversial (Jahn, 2004; Kröner et al., 2014; Safonova, 2017). A classical view of the CAOB holds that nearly half of the granites of the CAOB formed after the successive accretion of juvenile arc complexes and subduction accretion during the Phanerozoic (Sengör, 1990). Other view proposes that the Phanerozoic CAOB granitoids were the product of basaltic underplating in a post-collisional setting (Jahn et al., 2000; Wu et al., 2011). Nonetheless, the origins of the CAOB's granitoids might be far more complex. Some authors pointed out that many key features are explicable by Paleozoic ridge subduction (e.g. Windley and Xiao, 2018), and this model recently supported by local cases in the southwestern and southeastern CAOB (e.g., Tang et al., 2012; Li et al., 2021).

The Mongol-Okhotsk Ocean (MOO) was the youngest oceanic basin, which closure finalized the welding of CAOB terranes (Kravchinsky et al., 2002; Sorokin et al., 2020). The suturing of the MOO closure formed two volcanoplutonic belts in the territory of Mongolia: Selenge and Middle Gobi, on its northern and southern sides (in actual coordinates), respectively (Fig. 1; Zorin, 1999; Parfenov, 2001). The Middle Gobi Belt is thought to represent the southern active margin of the MOO (Fig. 1), however it remains a deficiency in detailed structural studies and up-to-date radiogenic ages and geochemical data. Consequently, the geodynamic evolution of the southern margin of the MOO and the reliable tectonic setting of the Middle Gobi Belt remains unclear. In this study, we present new zircon U–Pb ages, zircon Hf isotope and whole-rock geochemical and Nd isotope data from igneous rocks of the Mandalgovi volcanoplutonic suite of the Middle Gobi Belt. We will discuss the ages and tectonic settings of their emplacement, and petrogenesis in order to contribute to the better understanding of the crustal growth and tectonic evolution of the Middle Gobi Belt.

2. Geological setting

2.1 Geological background of Mongolia

Mongolia is located in the central CAOB (Fig. 1), and has recorded multiple episodes of orogeny during the Neoproterozoic to the Late Paleozoic (e.g., Badarch et al., 2002; Windley et al., 2007; Rojas-Agramonte et al., 2011). Geologically, Mongolia consists of a Northern Domain and a Southern Domain separated by the Main Mongolian Lineament (Tomurtogoo et al., 1998; Badarch et al., 2002; Fig. 1). The Northern Domain comprises Neoproterozoic–Early Paleozoic accretionary units and a collage of collided Precambrian blocks (Badarch et al., 2002; Xiao et al., 2003; Wilhem et al., 2012). The Southern Domain includes relicts of an extended long-lived subduction-accretionary system of the Paleo-Asian Ocean, which was active from the Neoproterozoic to the Permian (e.g., Demoux et al., 2009; Kröner et al., 2010; Batsaikhan et al., 2018). In Late Paleozoic to Mesozoic time, the Southern Domain approached and eventually docked with the Northern Domain to close MOO.

2.2 The Mongol–Okhotsk Belt

The Mongol–Okhotsk Belt extends from central Mongolia to the Okhotsk Sea over 3000 km. Its formation is linked with the evolution of the Mongol–Okhotsk Ocean (MOO), which existed between the Central Mongolia–Erguna block to the south, and the Siberian Craton to the north. The suture zone is marked by the ca. 325–314 Ma Adaatsag–Khukhu Davaa ophiolite belt (Tomurtogoo et al., 2005; Zhu et al., 2018) (Fig. 1). The MOO opened in late Ordovician–early Silurian times, possibly as a back-arc basin on the northern (in present coordinates) active margin of the Paleo-Asian Ocean near the Central Mongolia–Erguna block (Bussien et al., 2011; Miao et al., 2020; Wilfred et al., 2020). Other scientists suggested that the MOO opened much earlier in Neoproterozoic to Cambrian times (e.g., Zonenshain, 1990; Zorin, 1999).

The final closure of the MOO occurred in the Mesozoic (Jurassic to Cretaceous) as suggested by paleomagnetic data and the early Jurassic age of the youngest marine sediments (e.g., Cogné et al., 2005; Metelkin et al., 2010; Sorokin et al., 2020). So far, most scientists agree on the kinematic model of closure: a scissors-style, which is reflected by the younging trend of sediments and intrusions along the suture zone from west to east (e.g., Metelkin et al., 2010; Donskaya et al., 2013).

The Mongol–Okhotsk suture zone is bounded by the Khangay–Khentey accretionary terrane in the north-west (Fig. 1; Kelty et al., 2008; Bussien et al., 2011; Ruppen et al., 2014). The Khangay–Khentey terrane hosts all typical units of Ocean Plate Stratigraphy (OPS; from bottom to top): oceanic basalt (MORB, OIB), radiolarian pelagic chert, hemipelagic siliceous mudstone, siltstone, thick trench turbidite, and sandstone (e.g., Kelty et al., 2008; Safonova et al., 2009; Ruppen et al., 2014; Dagva-Ochir et al., 2020). The provenance analysis of sandstones and the U–Pb ages of detrital zircons show that the sediments of the northern part deposited from the Silurian to early Carboniferous times in a subduction-accretion setting, which apparently stopped in the Carboniferous. Later, subduction re-initiated during the Permian.

The Selenge and Middle Gobi belts are abutting with the Khangay–Khentey terrane (Fig. 1). Selenge Belt is believed to represent the northern, (Fig. 1), the Middle Gobi Belt is the southern active margin of the MOO (Zorin, 1999; Parfenov, 2001). The southern part of the Khangay–Khentey terrane experienced a back-arc extension during the Early Paleozoic (Bussien et al., 2011; Wilnkler et. al., 2020), and from the Devonian and to early Carboniferous it evolved as a passive margin. In the late Carboniferous, the subduction re-initiated resulting the transportation of detrital zircons from volcanic rocks and plutons of the Middle Gobi Belt until the Triassic (Kelty et al., 2008; Bussien et al., 2011).

2.3 The Middle Gobi Belt

The Middle Gobi Belt is a magmatic domain located south of the Mongol–Okhotsk suture (Fig. 1) (Badarch et al., 2002) and contains Precambrian basement rocks as bulk of the crust. The Precambrian basement consists of Meso–Neoproterozoic quartz-feldspathoid gneisses, metamorphic schists, pelitic gneisses, and metasandstones and marbles (Figs. 1, 2) overlain by the Silurian and Devonian marine sedimentary and volcanic rocks (turbiditic and pelagic series), which are intruded and overlapped by Permian plutonic and volcanic rocks, respectively (Badarch et al., 2002).

The Middle Gobi volcanoplutonic belt is dominated by Permian calc-alkaline andesites, dacites, rhyolites, trachyrhyolites and subalkaline granites (Khanchuk, 2015; Gerel et al., 2019). Several authors, according to shallow marine flysch deposit with volcanic horizons, considered the northern margin of the Middle Gobi Belt as a separate belt—North Gobi, representing a fossil forearc basin (Khanchuk et al., 2015) (Fig. 1). The emplacement of both ~270 Ma peraluminous granites and their associated volcanics, and ~240 Ma metaluminous granites (Machiowak et al., 2012; Gerel et al., 2019) was related to the subduction of the MOO lithosphere (e.g., Zhao et al., 2017; 2020). The late Triassic (~210 Ma) bimodal volcanic suites and coeval A-type granites were interpreted to form in a back-arc setting due to rollback of the MOO slab (Zhu et al., 2016).

The Mandalgovi volcanoplutonic suite occurs in the western fringe of the Middle Gobi Belt and occupies a large area of 250 × 650 km^2 (Fig. 2; Gerel et al., 2019). Devonian granites and volcanics are overlain unconformably by Carboniferous to Permian volcanics, volcanoclastics, clastic rocks and gneissic migmatites, which occur with Mandalgovi gabbro, gabbro-diorites, hornblende-granite and biotite-granite (Figs. 1c and 2; Badarch et al., 2002). Mafic dykes are abundant and occur associated with the Mandalgovi suite and sedimentary strata (Fig. 3). Pre-Mesozoic rocks are unconformably covered by Jurassic to Cretaceous sedimentary rocks (conglomerate, sandstone, and gravelite) and volcanics basalts, basaltic andesites, andesites and rhyolites) (Fig. 2).

3. Analytical methods

3.1 U–Pb geochronology

Zircon crystals were separated in the Graduate School of Science, Tohoku University, using standard techniques including conventional rock-crushing, magnetic and heavy liquid separation, and handpicking under a binocular microscope. Then, zircon crystals of similar size were mounted in epoxy discs. Zonation of zircon interiors was documented using cathodoluminescence (CL) imaging with a Hitachi S-3400N scanning electron microscope, equipped with a Gatan MiniCL. In-situ zircon U–Pb dating was carried out in the Okayama University of Science using a Thermo Fisher Scientific iCAP-RQ single-collector quadrupole coupled to a Teledyne Cetac Technologies Analyte G2 ArF excimer laser ablation (LA) system equipped with a HelEx 2 volume sample chamber. The laser ablation was conducted at the laser spot size of 25 μm, the fluence of 1.8 $J/cm^{2,}$ and the repetition rate of 5 Hz (for details see Aoki et al., 2019, 2020). Zircon standard Nancy 91500 (1065 Ma; Wiedenback et al., 2004) was used for age calibration, NIST SRM 612 standard (Jochum et al., 2011) for instrument optimization, and Plešovice zircons (337 Ma; Sláma et al., 2008) as secondary standards for quality control. U–Pb ages and concordia diagrams were, respectively, calculated and plotted using the programs IsoplotR (ver. 3.75; Vermeesch, 2018); concordia age of each sample incorporates errors on the decay constants and includes evaluation of concordance of apparent ages. The concordia ages and errors are at two-sigma level.

3.2 Whole-rock geochemistry

Eighteen samples were selected for whole-rock analysis. Concentrations of major and trace elements were measured at Activation Laboratories Ltd., Canada, using Code 4Litho Lithogeochemistry Package with fusion inductively coupled plasma optical emission spectrometry (FUS-ICPOES) and inductively coupled plasma mass spectroscopy (FUS-ICPMS), respectively. One more sample of was analyzed at the Analytical Center for Multi-Element and Isotope Studies of the Institute of Geology and Mineralogy, Novosibirsk, Russia. Major oxides were determined by the X-ray fluorescence (XRF) method using an Applied Research Laboratories ARL-9900-XP analyzer, following the standard procedure. Trace elements were analyzed by mass spectrometry with inductively coupled plasma (ICPMS) after fusion with $LiBO_2$. Simultaneous determination of all elements was carried out to low, medium, and high resolution, on a Finnigan Element-II high-resolution mass spectrometer with external calibration using BHVO-1 reference samples and an internal standard. The method has been validated through the analysis of nine reference materials. Relative standard deviations for all elements were <10% within the determined concentration ranges.

3.3 Zircon Hf isotopes

Hf isotope analysis was carried out using a Thermo Fisher Scientific Neptune Plus multi-collector (MC)-ICPMS in combination with a Geolas 2005 excimer ArF laser ablation system (193 nm) at the Institute of Geology and Geophysics, Chinese Academy of Science, Beijing. The analyses for zircon grains from the granites were conducted with a beam diameter of 63 μm, 6 Hz repetition rate, and energy of 15 mJ/cm^2. This setting yielded a signal intensity of 10 V at ^{180}Hf for the standard zircon Nancy 91500. Typical ablation time was 26 s, resulting in pits 20–30 μm deep. The initial ^{176}Hf/^{177}Hf ratios for the unknown samples were calculated to their initial value, using the measured ^{176}Lu/^{177}Hf ratios, the apparent age of each zircon grain, and an ^{176}Lu decay constant of 1.867×10^{-11} yr^{-1} (Söderlund et al., 2004). Epsilon Hf were calculated using a present-day chondritic $^{176}Hf/^{177}Hf$ value of 0.282785 and $^{176}Lu/^{177}Hf$ of 0.0336 (Bouvier et al., 2008) and the present-day felsic crustal ratio of $^{176}Lu/^{177}Hf = 0.015$.

3.4. Sm–Nd isotopic analysis

Sm–Nd isotopic analyses were performed at the Institute of Geology and Geochronology, Russian Academy of Sciences, Saint-Petersburg. About 100 mg of whole-rock powder was dissolved in a mixture of HF, HNO_3, and $HClO_4$. A ^{149}Sm–^{150}Nd spike solution was added to all samples before dissolution. REEs were separated on BioRad AGW50-X8 200–400 mesh resin using conventional cation-exchange techniques. Sm and Nd were separated by extraction chromatography with a LN-Spec (100–150 mesh) resin. The total blank in the laboratory was 0.1–0.2 ng for Sm and 0.1–0.5 ng for Nd. Isotopic compositions of Sm and Nd were determined on a TRITON TIMS mass-spectrometer. The precision (2σ) of Sm and Nd contents and $^{147}Sm/^{144}Nd$ ratios were 0.5% and 0.005% for $^{143}Nd/^{144}Nd$ ratios. $^{143}Nd/^{144}Nd$ ratios were adjusted relative to a value of 0.512115 for the JNdi-1standard. During the period of analysis, the weighted average of 10 JNdi-1 Nd standard runs yielded 0.512108 ± 7 (2σ) for $^{143}Nd/^{144}Nd$, normalized against $^{146}Nd/^{144}Nd = 0.7219$. The $\varepsilon_{Nd}(t)$ values were calculated using the present-day values for a chondritic uniform reservoir (CHUR) $^{143}Nd/^{144}Nd = 0.512638$ and $^{147}Sm/^{144}Nd = 0.1967$ (Jacobsen and Wasserburg, 1984). Whole-rock Nd model ages $T_{Nd(DM)}$ were calculated using the model of Goldstein and Jacobsen (1988) according to which the Nd isotopic composition of the depleted mantle evolved linearly since 4.56 Ga ago and has a present-day value $\varepsilon_{Nd}(0)$ of + 10 ($^{143}Nd/^{144}Nd = 0.513151$ and $^{147}Sm/^{144}Nd = 0.21365$). Two-stage (crustal) Nd model ages $T_{Nd(C)}$ were calculated using a mean crustal ratio $^{147}Sm/^{144}Nd$ of 0.12.

4. Results

4.1 Petrography

Gabbros (D0909) are coarse- to medium-grained gabbro-diorite with hypidiomorphic texture. The major minerals are plagioclase (50–55%), hornblende (25–30%), and biotite (15–20%) (Fig. 4). Euhedral to subhedral plagioclase exhibits polysynthetic twin zoning, kinking, and is partially replaced by sericite (Fig. 4a). Accessory minerals are ilmenite, magnetite, and apatite. Biotite-grained granites (D0906) is from a porphyritic biotite-granite (Fig. 4c). The major minerals include quartz (30–35%), plagioclase (30–35%), K-feldspar (20–25%), and biotite (15–20%). Plagioclase and K-feldspar occur as porphyritic minerals and biotite is common in fractures and along plagioclase boundaries (Fig. 4d). Accessory minerals are magnetite, apatite, and zircon. Hornblende-granites (D0914) are coarse- to fine-grained hypidiomorphic granodiorite consisting of subhedral to anhedral plagioclase (40–45%), K-feldspar (20–25%), subhedral quartz (15–20%), euhedral hornblende (15–20%), and biotite (5–10%) (Fig. 4e, f) plus accessory zircon and opaque minerals and secondary sericite and chlorite.

4.2 Whole-rock major and trace element geochemistry

Gabbro-diorite

This group of samples includes gabbro-diorite and diorite (Fig. 5a). They have relatively narrow spanned SiO_2 content (54–58 wt.%), high contents of MgO (4.08–4.34%), CaO (8.05–8.75%), FeO^T (6.10–7.9%), and Al_2O_3 (16.2–18.5%) and low total alkalis ($Na_2O + K_2O$ = 3.23–3.92%) (Fig. 5c). The contents of TiO_2 and P_2O_5 range from 0.77% to 0.79% and from 0.21% to 0.24%, respectively. The samples possess clear metaluminous features (Fig. 5d).

In terms of trace elements, the sample of gabbro-diorite display a comparably flat REE pattern [$(La/Yb)_N$ = 63–65] without significant Eu anomalies (Eu/Eu^* = 0.96–1.15) (Table 1; Fig. 6a), indicating no to weak fractionation and/or accumulation of plagioclase. They all have consistent primitive mantle-normalized patterns, characterized by lower Rb, Ba, Th, and U than the intermediate-felsic rocks of the same pluton, and characteristic troughs at Nb and Ta (Fig. 6b).

Biotite-granites

Biotite-granite rock group consists of granites and rhyolites (Fig. 5a, b) and have relatively narrow ranges of SiO_2 (69.8–77.9 wt.%), total alkalis ($Na_2O + K_2O$ = 6.7–8.21 wt.%) and Al_2O_3 (11.2–15.3 wt.%). They are characterized by low TiO_2 (0.05–0.26 wt.%), moderate FeO^T (0.84–0.96 wt.%), and Mg# (12–44.6). The samples are high-K calc-alkaline granites (Fig. 5c). According to the A/CNK vs. A/NK diagram they can be classified as peraluminous granitoids (Fig. 6d). The chondrite normalized REE patterns (Fig. 6c) show enrichment in LREEs [$(La/Yb)_{CN}$ = 0.7–3.6], and weak negative Eu anomalies. The multi-element patterns show negative Nb, P, and Ti anomalies (Fig. 6d) and significant enrichment in K, Rb, Ba, Pb.

Hornblende-granites

This group of samples include granodiorite and dacite with lower SiO_2 (61–70 wt.%), K_2O (1.91–3.99%), higher Al_2O_3 (13.7–17.3%), Na_2O (3.09–5.22%) and $K_2O + Na_2O$ (5.15–8.2%) than the biotite-granitoids. The samples are characterized by high FeO^T (3.09–6.08%), CaO (0.1–0.2%), TiO_2 (0.4–1%), and MgO (1.14–2.59%). Accordingly, they belong to the calc-alkaline to high calc-alkaline series (Fig. 6c; Table 1) and represent metaluminous granites (Fig. 5d).

In the CI-normalized REE diagrams (Fig. 6a), they exhibit various degrees of LREE enrichment with $(La/Yb)_N$ ratios of 3.5–25.4 and weak to zero negative anomalies at Eu ($Eu/Eu^* = 0.52–1.03$). In the PM-normalized spidergrams (Fig. 6d), all samples display patterns with enrichment of Rb, Th, K, La, Ce, and Zr and significant troughs at P and Ti.

4.3 .Geochronology

Biotite-granite (Sample D0906): Zircons were colorless or light yellow and are stubby or euhedral to anhedral, about 100–300 μm in size, elongation ratio 1 to 3. CL images show fine-scaled oscillatory zoning and rare unzoned xenocrystic cores (Fig. 7a). Fourteen analyses show the contents of U and Th varying from 67 μg/g to 175 μg/g and from 57 μg/g to 204 μg/g (Table 2), respectively, with Th/U ratios ranging from 0.6 to 1.2, suggesting a magmatic origin for the zircon (e.g., Kelly and Harley, 2005; Yakymchuk et al., 2018). The U–Pb ratios give a concordia age of 265 ± 2 Ma (MSWD = 0.19, Fig. 8a), which is interpreted as the crystallization age of biotite-granite.

Granodiorite (Sample D0914): Zircons are colorless or light brown, euhedral to subhedral, and stubby prisms up to 200 μm long with aspect ratios not exceeding 2 and exhibit fine oscillatory zoning (Fig. 7b). Sixteen analyses of zircons show the contents of U and Th varying from 143 μg/g to 236 μg/g and from 136 μg/g to 300 μg/g, respectively, and the ratios of Th/U ranging from 0.9 to 1.3. All analyses plotted on or near the concordia and yielded an age of 250 ± 3 Ma (MSWD = 1, Fig. 8b). This age is interpreted to represent the emplacement time of the granodiorite.

4.4 Nd–Hf isotopes

Seven analytical spots on the zircon grains/domains from the biotite-granite (Sample D0906) yielded initial $\varepsilon_{Hf}(t)$ values and two-stage model (T_{DM2}) ages ranging from + 5.07 to + 7.54 and from 775 to 898 Ma, respectively (Table 3). Eight analytical spots on zircon grains/domains from the granodiorite (Sample D0914) have $\varepsilon_{Hf}(t)$ values from + 4.47 to + 6.23 and T_{DM2} between 639 and 734 Ma. The whole-rock Nd isotope ratios yielded the values of $\varepsilon_{Nd}(t)$ at 0.4, which corresponds to a T_{DM2} of 877 Ma.

5. Discussion

5.1 Timing of magmatism

Based on lithostratigraphic relationships and K–Ar ages, previous researchers considered that the Mandalgovi volcanoplutonic suite of the Middle Gobi Belt consists of Neoproterozoic (Zaytsev and Luchitsky, 1979), early Cambrian, Devonian or early Permian (Gerel et al., 2012, 2019) formations. The state geological map shows the Mandalgovi biotite-granites as early Cambrian in age (Zaytsev and Luchitsky, 1979). Our new zircon U–Pb data demonstrate that these granitoids crystallized/emplaced during the Permian at ~265 Ma (Fig. 8). The designation of Precambrian age for the basement metamorphic rocks (Fig. 2) was mainly based on the intrusive relation between the so-called "early Cambrian" granites, where no precise radiogenic dating were performed previously. Therefore, reevaluating the age of the allegedly "Precambrian basement" metamorphic rocks in the future is needed.

5.2 Petrogenesis and magma sources

5.2.1 Biotite-granites

The Mandalgovi biotite-granites are characterized by high SiO_2, K, Rb, Pb, and low Na_2O, REE, and Sr, and high A/CNK (Fig. 5), and in the CaO/Na_2O vs. Al_2O_3/TiO_2 plot they fall in the field of peraluminous granites (Fig. 5d). Peraluminous, Si-rich granites can be produced by (1) partial melting of Al-rich metapelite and metagraywacke (Patiño Douce, 1999; Eyal et al., 2004; Healy et al., 2004); (2) partial melting of tonalite or granodiorite at pressures ≥ 8 kbar with restitic clinopyroxene (Patiño Douce, 1999); (3) mixing of the basaltic magma with terrigenous sediments. We did not observe wide range values of $\varepsilon_{Hf}(t)$ and $\varepsilon_{Nd}(t)$ nor abundance of the mafic microgranular enclaves within biotite-bearing granites, both being considered as an indicators of magma mixing and source heterogeneity, precluding the mixing model. The depletion of the granites in Sr, Nb, P, and Eu do suggest fractional crystallization (Fig. 6d). The negative Nb–Ti and P anomalies can be related to the fractionation of Ti-phases (ilmenite, titanite, etc.) and apatite, respectively. The Eu troughs in the REE spectra (Fig. 9c) and the Sr negative trend in the Ba vs. Sr and Sr vs. Eu diagrams (Fig. 9) indicate fractionation of plagioclase, i.e., shallow depth of melting. Compositions of biotite-granites are comparable with melts produced by dehydration-melting of various kinds of metasediments at low pressure (Fig. 10a), suggesting the derivation of their precursor magma from shallow crustal levels. This is consistent with the compositions of these granitoids which are close to the minimum point in the normative Qz–Ab–Or phase diagram ($P <$ 5 kbar) (Fig. 10b). This condition precludes the partial melting of the tonalite at the pressures $P \geq$ 8 kbar. In the diagrams of $(Na_2O + K_2O)/(FeO^T + TiO_2)$ vs. $(Na_2O + K_2O + FeO^T + MgO + TiO_2)$ and $Al_2O_3/(MgO + FeO^T)$ vs. $CaO/(MgO + FeO^T)$ diagrams indicate partial melting of a metagraywacke source for generating the biotite-granitic magma (Fig. 11). The Rb/Ba vs. Rb/Sr ratios indicate that the source magma was from clay-poor melts in a shallow depths (Fig. 11c).

5.2.2 Hornblende-granites

The Mandalgovi hornblende-granites are classified as metaluminous granitoids (Fig. 5). In general, calc-alkaline metaliuminous granites form by assimilation and fractional crystallization of mantle-derived basaltic sources, mixing of mafic magma with crust-derived felsic magma, or partial melting of juvenile mafic crust (e.g., Chappell and White, 2001; Kemp et al., 2007; Clemens et al., 2011; Moyen et al., 2017). Metaluminous granites generated by magma mixing typically carry abundant mafic enclaves and have a variable chemical composition (e.g., Chappell, 1996), which is not observed in our samples. Na-rich ($Na_2O/K_2O > 1$), high-Al_2O_3 melts with intermediate to silicic compositions may be produced by ~20–40% dehydration melting of metabasalts at temperatures between 1050 and 1100 °C, leaving a granulite residue at 8–12 kbar and garnet granulite to eclogite residues at 12–32 kbar (Rapp and Watson, 1995; Rapp, 1995). However, unlike the biotite-granites, show no notable trends of fractionation (Fig. 9a, b), thus excluding the partial melting scenario. The Mandalgovi hornblende-granitoids have low K and Th; and dominated by intermediate compositions, which are consistent with those of experimental melts derived by the dehydration melting of metabasalts or amphibolite (Figs. 11a–c). Therefore, we think that the Mandalgovi hornblende-granites formed by the partial melting of mafic protoliths.

5.2.3 Gabbro-diorites

Gabbro-diorites are mostly tholeiitic and characterized by low SiO_2 and total alkali, but high MgO, FeO^T and CaO but enriched in LREE and LILE and depleted in HREEs and HFSEs. Those geochemical features are typical of arc magmas. In addition, those features can result from crustal contamination, since the average lithospheric mantle and continental crust are both depleted in Nb and Ta relative to neighboring elements (Th, La) (Rudnick and Gao, 2003). However, significant crustal contamination leads not only to Nb–Ta depletion but also increases concentrations of Zr and Hf, giving rise to negative Nb–Ta anomalies and positive Zr–Hf anomalies in mantle-normalized trace element spidergrams (Fig. 6b) (Zhao and Zhou, 2009). The Mandalgovi gabbro-diorites display troughs at Nb–Ta, and Zr, and peaks at Pb, which cannot be completely attributed to crustal contamination, but could indicate arc-derived magmatism.

Nb is commonly depleted in the lithospheric mantle relative to La, so low Nb/La ratios (<0.5) for mafic magmas suggest a lithospheric mantle source and higher ratios (>1) indicate an OIB-like asthenospheric mantle source (Smith et al., 1999). The Nb/La ratios for the gabbro-diorites are between 0.1 and 0.3, i.e. closer to the lithospheric mantle source.

5.3 Tectonic implications

The Mandalgovi suite of the Middle Gobi Belt hosts spatially and temporally associated peraluminous biotite-granite, metaluminous hornblende-granite igneous rocks and gabbro-diorites. The formation of peraluminous granites is generally attributed to collisional and/or post-collisional settings (Barbarin 1996, 1999; Chappell et al., 2011). A normal crustal thickness of 15–20 km was suggested in the Central Mongolia in the Paleozoic by Zorin et al. (1993), which is distinct from collisional orogens with overthickened crust. Additionally, the small amount of peraluminous granites and absence of detachment fault zones, gneiss dome and metamorphic core complexes, usually associated to the post-collisional granites are indicate that they were not formed in a post-collisional setting (Fig. 2). Moreover, studies showed that continuous subduction-related widespread magmatism in the Central Mongolia from early Permian and to the late Triassic (e.g., Ganbat et al., 2021b), and possible post-collisional granites appeared after ca. 220 Ma (Fig. 12; Zhu et al., 2016)

Normal oceanic crust subduction may hardly provide sufficient heat for partial melting of metasedimentary rocks in a shallow depth, and their generation requires specific geothermal condition (e.g., Zhang et al., 2004).

More recent studies proposed that peraluminous granites could also form in other geodynamic scenarios that provide an enhanced thermal gradient to the crust facilitating crustal melting including: ridge subduction (Cai et al., 2011; Kong et al., 2019), mantle plumes (Li et al., 2011).

Alternative studies proposed back-arc extension model to facilitate the generation of S-type granites in the New England orogen of circum-Pacific (Collins and Richards, 2008; Collins et al., 2020). This model suggests that back-arc extension is induced by repeated, long-term subduction retreat and the sediment-dominated back-arc basin is triggered to melt when hot basaltic magmas intruded into the thinned back-arc crust once slab retreat is re-established. Such a setting requires a long history of subduction before the extension to provide crustal thickening before the formation of peraluminous granites, flat subduction initiation, and subsequent rollback (Collins and Richards, 2008). We decline such a scenario as the peraluminous granites of the Middle Gobi Belt emplaced in the fore-arc setting (Fig. 1). The positive zircon $\varepsilon_{Hf}(t)$ values and whole-rock $\varepsilon_{Nd}(t)$ isotopic values observed in peraluminous samples make them distinct from classical peraluminous granites (Fig. 12), and are generally interpreted to require an extreme heat source (Appleby et al., 2010; Liu and Zhao, 2018). These characters also are typical of greywackes formed by destruction of juvenile igneous rocks formed at intra-oceanic arcs (Safonova et al., 2017, 2021). Therefore, we suggest that the peraluminous granites may have formed by melting of the sediments in a fore-arc setting of an intraoceanic arc.

After ~250 Ma, peraluminous granitoids were supplanted by calc-alkaline metaluminous granites and gabbro-diorites, where they took place when by parental magmas being derived from the melting of the lithospheric mantle or juvenile mafic lower crustal sources, which led by downgoing oceanic slab.

Medium to high-K calc-alkaline metaluminous granites can form in two tectonic settings: (1) post-collisional settings similar to the Caledonides (e.g., Litvinovsky et al., 2021), (2) continental arcs similar to the Andes (Roberts and Clemens, 1993), and (3) intraoceanic arcs similar to the Japanese and Aleutian islands (Kay et al., 1990). We preclude the post-collisional setting because there is no evidence for the Permian intra-plate magmatism and post-collisional detachment fault in the study area. The ~250 Ma igneous association lacks abundant felsic magmas (rhyolites) which occur rather as pyroclastic flow material derived from a continental margin (Kay et al., 1990; Wilson, 2007) (Fig. 2). Additionally, they have lower concentrations of K_2O, Pb, Sr, Rb, Ba, Th, and U than those formed in an Andean-type active continental margin (Fig. 6b).

Their neutral to positive $\varepsilon_{Hf}(t)$ (+0.4 to +7.5) and $\varepsilon_{Nd}(t)$ (0.4) characteristics and the T_{DM2} of 775 to 1019 Ma (Table 3) suggest the generation of primary magmas by the partial melting of a relatively depleted juvenile lower crust or depleted mantle source. Detrital zircon $\varepsilon_{Hf}(t)$ value from the northern margin of the Middle Gobi Belt also exhibits mostly positive $\varepsilon_{Hf}(t)$ (–7 to +14) (Bussien et al., 2011; Wilfred et al., 2020), with slightly negative values, implying that the crustal development occurred on the mature arc. Based on the above evidence, we conclude that the ~250 Ma granitoids and gabbro-diorites of the Mandalgovi pluton formed in an intra-oceanic subduction setting.

The abundance of hornblende and the incompatible trace element composition of the Mandalgovi gabbro-diorites suggest that they were generated in a subduction-related tectonic setting. In the tectonic discrimination diagrams for mafic rocks gabbro-diorites plot in the field of island arc (Fig. 13a, b). Their association with hornblende-granitoids (Fig. 2) and linear trend from tholeiitic to high-K calc-alkaline series suggest close ages of the two units. The emplacement of the peraluminous granites and coeval volcanic rocks was short after the peak of voluminous subduction-related metaluminous granites (after ~15 Ma; Fig. 12).

Normal oceanic crust subduction may hardly provide sufficient heat for partial melting of metasedimentary rocks in a shallow depth, and their generation requires specific geothermal condition. Mafic–intermediate dykes, and the presence of migmatites (Fig. 3) were associated which peraluminous granites and sedimentary strata also may require extreme heat source.

A ridge subduction is probably viable scenario for the tectonic setting of the Mandalgovi suite. Ridge subduction impacts strongly on magmatic activity, metamorphism and mineralization near convergent plate margins (Thorkelson, 1996; Sisson, 2003). When the ridge intersects with the subduction zone, a “slab window” will form between the subducted parts of the diverging oceanic plates (Dickinson and Snyder, 1979; Thorkelson, 1996). The upwelling of asthenospheric mantle through the slab window provides high heat flow that can induce partial melting of the slab edge, overlying mantle wedge and/or upwelling asthenospheric mantle and crustal rocks, and can produce a wide variety of magmas (e.g., Sisson et al., 2003). Ridge subduction in the CAOB was introduced by Windley et al. (2007) and it was one of the most remarkable tectonic setting that responsible for the many key features of the CAOB, as the modern circum-Pacific accretionary orogens (Liu et al., 2020; Ganbat et al., 2021c).

Thus, we suggest that the Permian oceanic ridge subduction caused anomalies of thermal and physical conditions in the surrounding mantle and upwelling of asthenosphere, triggered partial melting metasedimentary rocks which was derived from pre-Permian mature arc (Miao et al., 2020; Wilfred et al., 2020) in the forearc setting in a shallow depth. Intrusion of mafic–intermediate dykes into the accretionary prism and supports the ridge subduction and slab window model (Sisson et al., 2003; Windley et al., 2007). The mafic crust was the source for metaluminous granitoids. Although our study was confined to a relatively small area in the central part of the CAOB (Fig. 1), it supports the view that ridge subduction was common during formation of the entire belt.

In the early-Carboniferous (ca. 325 Ma), the southward subduction of the MOO lithosphere started to form the Adaatsag and Khuhu Davaa ophiolites (Fig. 1). Two subduction zones were proposed at the southern margin of the MOO, which generated two arcs: intra-oceanic arc (Onon) and continental arc (Ereendavaa, Middle Gobi) (e.g., Zhu et al., 2018; Miao et al., 2020). However, there is no evidence of coeval or younger accretionary wedge, which should be an integral constituent of an intra-oceanic arc system and direct evidence for an arc except for the late Carboniferous detrital zircons. The positive $\varepsilon_{Hf}(t)$ values of the detrital zircons may suggest tectonic erosion of former magmatic arc rocks, as those in NE Japan (Safonova et al., 2015; Pastor-Galán et al., 2021). The Middle Gobi Belt has been previously considered as a Permian–Triassic Andean-type active continental margin terrane (Parfenov, 2001; Tomurtogoo et al. 2005; Zhu et al., 2016). Our results show that the tectonic history of the Middle Gobi Belt is more complex than previously thought and that the Mandalgovi suite could have formed in an intra-oceanic arc setting with ridge subduction, but we still cannot exclude a continental margin setting for the whole belt. The northern margin of the Middle Gobi Belt, the North Gobi, could have formed in a fore-arc of the MOO, as well (Khanchuk et al., 2015).

During the ~265 Ma, the Mongol–Okhotsk Oceanic ridge subducted beneath the arc. As the slab window opened, the upwelling asthenosphere heated and then melted the overlying fore-arc sediments and induced to generate peraluminous granites. The mafic dykes in the Mandalgovi batholiths probably formed from the partial melting of a refractory mantle with previous magma extraction. This is also supported by migmatite occurrence adjacent to the batholith (Fig. 3). Later, at ~250 Ma, metaluminous granitoids and gabbro-diorites of the Mandalgovi pluton formed in an intra-oceanic subduction of the Mongol–Okhotsk Ocean.

Previous studies show that the CAOB may contain many examples of ridge subduction and slab windows, for example in the Junggar and the Chinese Altai, and in East Junggar, Beishan, the Tianshan, the Russian Altai, and in Inner Mongolia (Windley and Xiao, 2018). Ridge subduction may have caused extensive underplating/intraplating of hot mantle-derived basaltic magma as a result of asthenosphere upwelling, which could have provided not only sufficient heat for the widespread crustal melting, but also significant juvenile materials for the crustal growth in the CAOB.

6. *Conclusions*

Based on the obtained result we draw the following conslusions:

1. The Mandalgovi suite consists of peraluminous and metaluminous granitoids, their volcanic counterparts, and gabbro-diorites.
2. The Mandalgovi peraluminous granites emplaced at ~265 Ma and derived by partial melting from metagraywacke in a fore-arc setting just above the slab window produced after the mid-ocean ridge subduction.
3. The Mandalgovi metaluminous granitoids were emplaced at ~250 Ma and resulted from the partial melting of a metabasaltic source in an intra-oceanic arc setting.
4. The Mandalgovi gabbro-diorites were formed by partial melting of a metasomatized lithospheric mantle source in a supra-subduction setting.
5. The northern margin of the Middle Gobi Belt may include both intra-oceanic setting above the subducted ridge and active continental margin terranes of the Mongol–Okhotsk Ocean.

6. Acknowledgment

This research was supported by CNEAS and FRIS of Tohoku University and in part by grants from the MEXT/JSPS KAKENHI JP18H01299 and JP21H01174 to Tatsuki Tsujimori and JP19K04043 to Kazumasa Aoki, by the National Natural Science Foundation of China (grant number 41772230) to Laicheng Miao, and by the Russian

Science Foundation (21-77-20022; Nd isotope studies) to Inna Safonova. Ari Ganbat gratefully acknowledges the Japanese Government MEXT Scholarship. We also thank Isamu Morita and Otgonbayar Dandar for their assistance in the laboratory and for providing geological material. Contribution to IGCP#662.

ORCID

Ariuntsetseg Ganbat https://orcid.org/ 0000-0003-2464-4161
Tatsuki Tsujimori https://orcid.org/0000-0001-9202-7312
Laicheng Miao https://orcid.org/ 0000-0001-6296-4444
Inna Safonova https://orcid.org/ 0000-0003-2464-4161
Daniel Pastor-Galán https://orcid.org/ 0000-0002-0226-2739
Chimedtseren Anaad https://orcid.org/ 0000-0001-7878-0738
Shogo Aoki https://orcid.org/ 0000-0001-5093-1346
Kazumasa Aoki https://orcid.org/ 0000-0001-7645-6766

REFERENCES

Appleby, S. K., Gillespie, M. R., Graham, C. M., Hinton, R. W., Oliver, G. J., & Kelly, N. M. (2010). Do S-type granites commonly sample infracrustal sources? New results from an integrated O, U–Pb and Hf isotope study of zircon. *Contributions to Mineralogy and Petrology*, *160*(1), 115-132.

Armstrong, R. L. (1981). Radiogenic isotopes: the case for crustal recycling on a near-steady-state no-continental-growth Earth. *Philosophical Transactions of the Royal Society of London. Series A, Mathematical and Physical Sciences*, *301*(1461), 443-472.

Badarch, G., Cunningham, W. D., & Windley, B. F. (2002). A new terrane subdivision for Mongolia: implications for the Phanerozoic crustal growth of Central Asia. Journal of Asian Earth Sciences, 21(1), 87-110.

Barbarin, B. (1996). Genesis of the two main types of peraluminous granitoids. Geology, 24(4), 295-298

Barbarin, B. (1999). A review of the relationships between granitoid types, their origins and their geodynamic environments. Lithos, 46(3), 605-626.

Batsaikhan, U., Noriyoshi, T., Anaad, C., & Bayaraa, B. (2018). Petrochemical characteristics of late Paleozoic magmatic rocks of the Mandakh area, southeast Mongolia. Mongolian Geoscientist, (47), 5-21.

Belousova, E. A., Kostitsyn, Y. A., Griffin, W. L., Begg, G. C., O'Reilly, S. Y., & Pearson, N. J. (2010). The growth of the continental crust: constraints from zircon Hf-isotope data. *Lithos*, *119*(3-4), 457-466.

Bouvier, A., Vervoort, J. D., & Patchett, P. J. (2008). The Lu–Hf and Sm–Nd isotopic composition of CHUR: constraints from unequilibrated chondrites and implications for the bulk composition of terrestrial planets. *Earth and Planetary Science Letters*, *273*(1-2), 48-57.

Buslov, M. M., Saphonova, I. Y., Watanabe, T., Obut, O. T., Fujiwara, Y., Iwata, K., & Kazansky, A. Y. (2001). Evolution of the Paleo-Asian Ocean (Altai-Sayan Region, Central Asia) and collision of possible Gondwana-derived terranes with the southern marginal part of the Siberian continent. *Geosciences Journal*, *5*(3), 203-224.

Bussien, D., Gombojav, N., Winkler, W., & Von Quadt, A. (2011). The Mongol–Okhotsk Belt in Mongolia—an appraisal of the geodynamic development by the study of sandstone provenance and detrital zircons. *Tectonophysics*, *510*(1-2), 132-150.

Cai, K., Sun, M., Yuan, C., Zhao, G., Xiao, W., Long, X., & Wu, F. (2011). Geochronology, petrogenesis and tectonic significance of peraluminous granites from the Chinese Altai, NW China. *Lithos*, *127*(1-2), 261-281.

Chappell, B. W. (1996). Magma mixing and the production of compositional variation within granite suites: evidence from the granites of southeastern Australia. *Journal of petrology*, *37*(3), 449-470.

Chappell, B. W., & White, A. J. (2001). Two contrasting granite types: 25 years later. *Australian journal of earth sciences*, *48*(4), 489-499.

Cogné, J. P., Kravchinsky, V. A., Halim, N., & Hankard, F. (2005). Late Jurassic-Early Cretaceous closure of the Mongol-Okhotsk Ocean demonstrated by new Mesozoic palaeomagnetic results from the Trans-Baikal area (SE Siberia). *Geophysical Journal International*, *163*(2), 813-832.

Collins, W. J., & Richards, S. W. (2008). Geodynamic significance of S-type granites in circum-Pacific orogens. *Geology*, *36*(7), 559-562

Collins, W. J., Huang, H. Q., Bowden, P., & Kemp, A. I. S. (2020). Repeated S–I–A-type granite trilogy in the Lachlan Orogen and geochemical contrasts with A-type granites in Nigeria: implications for petrogenesis and tectonic discrimination. *Geological society, london, special publications*, *491*(1), 53-76.

Clemens, J. D., Stevens, G., & Farina, F. (2011). The enigmatic sources of I-type granites: the peritectic connexion. *Lithos*, *126*(3-4), 174-181.

Dagva-Ochir, L., Oyunchimeg, T. U., Enkhdalai, B., Safonova, I., Li, H., Otgonbaatar, D., Tamehe, S., & Sharav, D. (2020). Middle Paleozoic intermediate-mafic rocks of the Tsoroidog Uul'accretionary complex, Central Mongolia: Petrogenesis and tectonic implications. *Lithos*, *376*, 105795.

Demoux, A., Kröner, A., Liu, D., & Badarch, G. (2009). Precambrian crystalline basement in southern Mongolia as revealed by SHRIMP zircon dating. *International Journal of Earth Sciences*, *98*(6), 1365-1380.

Dickinson, W. R., & Snyder, W. S. (1979). Geometry of subducted slabs related to San Andreas transform. *The Journal of Geology*, *87*(6), 609-627.

Dobretsov, N. L., Berzin, N. A., & Buslov, M. M. (1995). Opening and tectonic evolution of the Paleo-Asian Ocean. *International Geology Review*, *37*(4), 335-360

Donskaya, T. V., Gladkochub, D. P., Mazukabzov, A. M., & Ivanov, A. V. (2013). Late Paleozoic–Mesozoic subduction-related magmatism at the southern margin of the Siberian continent and the 150 million-year history of the Mongol-Okhotsk Ocean. *Journal of Asian Earth Sciences*, *62*, 79-97.

Eyal, M., Litvinovsky, B. A., Katzir, Y., & Zanvilevich, A. N. (2004). The Pan-African high-K calc-alkaline peraluminous Elat granite from southern Israel: geology, geochemistry and petrogenesis. *Journal of African Earth Sciences*, *40*(3-4), 115-136.

Ganbat, A., Tsujimori, T., Boniface, N., Pastor-Galán, D., Aoki, S., & Aoki, K. (2021a). Crustal evolution of the Paleoproterozoic Ubendian Belt (SW Tanzania) western margin: A Central African Shield amalgamation tale. *Gondwana Research*, *91*, 286-306.

Ganbat, A., Tsujimori, T., Miao, L., Safonova, I., Pastor-Galán, D., Anaad, C., Baatar, M. & Savinskiy, I. (2021b). Late Paleozoic–Early Mesozoic granitoids in the Khangay-Khentey basin, Central Mongolia: Implication for the tectonic evolution of the Mongol-Okhotsk Ocean margin. *Lithos*, 106455

Ganbat, A., Pastor-Galán, D., Hirano, N., Nakamura, N., Sumino, H., Yamaguchi, Y., & Tsujimori, T. (2021c). Cretaceous to Miocene NW Pacific Plate Kinematic Constraints: Paleomagnetism and Ar–Ar Geochronology in the Mineoka Ophiolite Mélange (Japan). *Journal of Geophysical Research: Solid Earth*, *126*(5), e2020JB021492.

Gerel, O., Batkhishig, B., Munkhtsengel, B., & Javkhlan, O. (2019). Geochemistry and geochronology of Mandalgovi Complex. Mongolian Geoscientist (In Mongolian with English abstract), 48.

Goldstein, S. J., & Jacobsen, S. B. (1988). Nd and Sr isotopic systematics of river water suspended material: implications for crustal evolution. *Earth and Planetary Science Letters*, *87*(3), 249-265

Halder, M., Paul, D., & Sensarma, S. (2021). Rhyolites in continental mafic Large Igneous Provinces: Petrology, geochemistry and petrogenesis. *Geoscience Frontiers*, *12*(1), 53-80.

Hawkesworth, C. J., Dhuime, B., Pietranik, A. B., Cawood, P. A., Kemp, A. I., & Storey, C. D. (2010). The generation and evolution of the continental crust. *Journal of the Geological Society*, *167*(2), 229-248

Healy, B., Collins, W. J., & Richards, S. W. (2004). A hybrid origin for Lachlan S-type granites: the Murrumbidgee Batholith example. *Lithos*, *78*(1-2), 197-216.

Irvine, T. N., & Baragar, W. R. A. (1971). A guide to the chemical classification of the common volcanic rocks. *Canadian journal of earth sciences*, *8*(5), 523-548.

Jahn, B. M., Wu, F., & Chen, B. (2000). Massive granitoid generation in Central Asia: Nd isotope evidence and implication for continental growth in the Phanerozoic. *Episodes*, *23*(2), 82-92.

Jahn, B. M. (2004). The Central Asian Orogenic Belt and growth of the continental crust in the Phanerozoic. *Geological Society, London, Special Publications*, *226*(1), 73-100

Jacobsen, S. B., & Wasserburg, G. J. (1984). Sm-Nd isotopic evolution of chondrites and achondrites, II. *Earth and Planetary Science Letters*, *67*(2), 137-150.

Jochum, K. P., Weis, U., Stoll, B., Kuzmin, D., Yang, Q., Raczek, I., & Enzweiler, J. (2011). Determination of reference values for NIST SRM 610–617 glasses following ISO guidelines. *Geostandards and Geoanalytical Research*, *35*(4), 397-429.

Kay, S. M., Kay, R. W., Citron, G. P., & Perfit, M. R. (1990). Calc-alkaline plutonism in the intra-oceanic Aleutian arc, Alaska. *Plutonism from Antarctica to Alaska: Geological Society of America Special Paper*, *241*, 233-255.

Kelly, N. M., & Harley, S. L. (2005). An integrated microtextural and chemical approach to zircon geochronology: refining the Archaean history of the Napier Complex, east Antarctica. *Contributions to Mineralogy and Petrology*, *149*(1), 57-84.

Kelty, T. K., Yin, A., Dash, B., Gehrels, G. E., & Ribeiro, A. E. (2008). Detrital-zircon geochronology of Paleozoic sedimentary rocks in the Hangay–Hentey basin, north-central Mongolia: implications for the tectonic evolution of the Mongol–Okhotsk Ocean in central Asia. *Tectonophysics*, *451*(1-4), 290-311.

Kemp, A. I. S., Hawkesworth, C. J., Foster, G. L., Paterson, B. A., Woodhead, J. D., Hergt, J. M., Gray.C & Whitehouse, M. J. (2007). Magmatic and crustal differentiation history of granitic rocks from Hf-O isotopes in zircon. *Science*, *315*(5814), 980-983.

Khanchuk, A., Didenko, A., Popeko, L., Sorokin, A., Shevchenko, B. (2017). Structure and Evolution of the Mongol-Okhotsk Belt, in Kröner, A. The Central Asian Orogenic Belt. *The Leading Edge*, *36*(7).

Kong, X., Zhang, C., Liu, D., Jiang, S., Luo, Q., Zeng, J., ... & Wang, X. (2019). Disequilibrium partial melting of metasediments in subduction zones: Evidence from O-Nd-Hf isotopes and trace elements in S-type granites of the Chinese Altai. *Lithosphere*, *11*(1), 149-168.

Kravchinsky, V. A., Cogné, J. P., Harbert, W. P., & Kuzmin, M. I. (2002). Evolution of the Mongol-Okhotsk Ocean as constrained by new palaeomagnetic data from the Mongol-Okhotsk suture zone, Siberia. *Geophysical Journal International*, *148*(1), 34-57.

Kröner, A., Lehmann, J., Schulmann, K., Demoux, A., Lexa, O., Tomurhuu, D., Štípská, P., Liu, D., & Wingate, M. T. (2010). Lithostratigraphic and geochronological constraints on the evolution of the Central Asian Orogenic Belt in SW Mongolia: Early Paleozoic rifting followed by late Paleozoic accretion. *American Journal of Science*, *310*(7), 523-574.

Kröner, A., Kovach, V., Belousova, E., Hegner, E., Armstrong, R., Dolgopolova, A., & Rytsk, E. (2014). Reassessment of continental growth during the accretionary history of the Central Asian Orogenic Belt. *Gondwana Research*, *25*(1), 103-125.

Kröner, A., Kovach, V., Alexeiev, D., Wang, K. L., Wong, J., Degtyarev, K., & Kozakov, I. (2017). No excessive crustal growth in the Central Asian Orogenic Belt: Further evidence from field relationships and isotopic data. *Gondwana Research*, *50*, 135-166.

Le Bas, M. J., Rex, D. C., & Stillman, C. J. (1986). The early magmatic chronology of Fuerteventura, Canary Islands. *Geological Magazine*, *123*(3), 287-298.

Li, Z., Chen, H., Song, B., Li, Y., Yang, S., & Yu, X. (2011). Temporal evolution of the Permian large igneous province in Tarim Basin in northwestern China. *Journal of Asian Earth Sciences*, *42*(5), 917-927.

Li, J., Liu, J., Wang, Y., Zhu, D. C., & Wu, C. (2021). Late Carboniferous to Early Permian ridge subduction identified in the southeastern Central Asian Orogenic Belt: Implications for the architecture and growth of continental crust in accretionary orogens. *Lithos*, *384*, 105969.

Liu, H., & Zhao, J. H. (2018). Neoproterozoic peraluminous granitoids in the Jiangnan Fold Belt: Implications for lithospheric differentiation and crustal growth. *Precambrian Research*, *309*, 152-165.

Liu, K., Zhang, J., Xiao, W., Wilde, S. A., & Alexandrov, I. (2020). A review of magmatism and deformation history along the NE Asian margin from ca. 95 to 30 Ma: Transition from the Izanagi to Pacific plate subduction in the early Cenozoic. *Earth-Science Reviews*, 103317.

Litvinovsky, B. A., Vapnik, Y., Eyal, M., & Eyal, Y. (2021). The role of mantle and the ancient continental crust in the generation of post-collisional high-K calc-alkaline and alkaline granites, with main reference to the Arabian-Nubian Shield. *Lithos*, *388*, 106049.

Machowiak, K., Stawikowski, W., & Achramowicz, S. (2012). Late Triassic ^{40}Ar-^{39}Ar ages of the Baga-Gazryn Chuluu granites (Central Mongolia). *Journal of Geosciences*, *57*(3), 173-188.

Maniar, P. D., & Piccoli, P. M. (1989). Tectonic discrimination of granitoids. *Geological society of America bulletin*, *101*(5), 635-643.

Metelkin, D. V., Vernikovsky, V. A., Kazansky, A. Y., & Wingate, M. T. (2010). Late Mesozoic tectonics of Central Asia based on paleomagnetic evidence. *Gondwana Research*, *18*(2-3), 400-419.

Miao, L., Zhu, M., Liu, C., Baatar, M., Anaad, C., Yang, S., & Li, X. (2020). Detrital-Zircon Age Spectra of Neoproterozoic-Paleozoic Sedimentary Rocks from the Ereendavaa Terrane in NE Mongolia: Implications for the Early-Stage Evolution of the Ereendavaa Terrane and the Mongol-Okhotsk Ocean. *Minerals*, *10*(9), 742.

Moyen, J. F., Laurent, O., Chelle-Michou, C., Couzinié, S., Vanderhaeghe, O., Zeh, A., ... & Gardien, V. (2017). Collision vs. subduction-related magmatism: two contrasting ways of granite formation and implications for crustal growth. *Lithos*, *277*, 154-177.

Parfenov, L. M., Popeko, L. I., & Tomurtogoo, O. (2001). Problems of tectonics of the Mongol-Okhotsk orogenic belt.

Pastor-Galán, D., Spencer, C. J., Furukawa, T., & Tsujimori, T. (2021). Evidence for crustal removal, tectonic erosion and flare-ups from the Japanese evolving forearc sediment provenance. *Earth and Planetary Science Letters*, *564*, 116893.

Patiño Douce, A. E., & Harris, N. (1998). Experimental constraints on Himalayan anatexis. *Journal of Petrology*, *39*(4), 689-710.

Patiño Douce, A. E. (1999). What do experiments tell us about the relative contributions of crust and mantle to the origin of granitic magmas?. *Geological Society, London, Special Publications*, *168*(1), 55-75.

Patiño Douce, A. E., & Johnston, A. D. (1991). Phase equilibria and melt productivity in the pelitic system: implications for the origin of peraluminous granitoids and aluminous granulites. *Contributions to Mineralogy and Petrology*, *107*(2), 202-218.

Pearce, T. H., Gorman, B. E., & Birkett, T. C. (1977). The relationship between major element chemistry and tectonic environment of basic and intermediate volcanic rocks. *Earth and Planetary Science Letters*, *36*(1), 121-132.

Peccerillo, A., & Taylor, S. R. (1976). Geochemistry of Eocene calc-alkaline volcanic rocks from the Kastamonu area, northern Turkey. *Contributions to mineralogy and petrology*, *58*(1), 63-81.

Rapp, R. P., & Watson, E. B. (1995). Dehydration melting of metabasalt at 8–32 kbar: implications for continental growth and crust-mantle recycling. *Journal of Petrology*, *36*(4), 891-931.

Rapp, R. P. (1995). Amphibole-out phase boundary in partially melted metabasalt, its control over liquid fraction and composition, and source permeability. *Journal of Geophysical Research: Solid Earth*, *100*(B8), 15601-15610.

Rino, S., Kon, Y., Sato, W., Maruyama, S., Santosh, M., & Zhao, D. (2008). The Grenvillian and Pan-African orogens: world's largest orogenies through geologic time, and their implications on the origin of superplume. *Gondwana Research*, *14*(1-2), 51-72.

Roberts, M. P., & Clemens, J. D. (1993). Origin of high-potassium, calc-alkaline, I-type granitoids. *Geology*, *21*(9), 825-828.

Rojas-Agramonte, Y., Kröner, A., Demoux, A., Xia, X., Wang, W., Donskaya, T., ... & Sun, M. (2011). Detrital and xenocrystic zircon ages from Neoproterozoic to Palaeozoic arc terranes of Mongolia: significance for the origin of crustal fragments in the Central Asian Orogenic Belt. *Gondwana Research*, *19*(3), 751-763.

Rosenbaum, G. (2018). The Tasmanides: Phanerozoic tectonic evolution of eastern Australia. *Annual Review of Earth and Planetary Sciences*, *46*, 291-325.

Rudnick, R. L., Gao, S., Holland, H. D., & Turekian, K. K. (2003). Composition of the continental crust. *The crust*, *3*, 1-64.

Ruppen, D., Knaf, A., Bussien, D., Winkler, W., Chimedtseren, A., & von Quadt, A. (2014). Restoring the Silurian to Carboniferous northern active continental margin of the Mongol–Okhotsk Ocean in Mongolia: Hangay–Hentey accretionary wedge and seamount collision. *Gondwana Research*, *25*(4), 1517-1534.

Safonova, I. Y., Utsunomiya, A., Kojima, S., Nakae, S., Tomurtogoo, O., Filippov, A. N., & Koizumi, K. (2009). Pacific superplume-related oceanic basalts hosted by accretionary complexes of Central Asia, Russian Far East and Japan. *Gondwana Research*, *16*(3-4), 587-608.

Safonova, I., Seltmann, R., Kroner, A., Gladkochub, D., Schulmann, K., Xiao, W., Kim, J., Komiya, Ts. & Sun, M. (2011). A new concept of continental construction in the Central Asian Orogenic Belt. *Episodes*, *34*(3), 186-196.

Safonova, I., Maruyama, S., & Litasov, K. (2015). Generation of hydrous-carbonated plumes in the mantle transition zone linked to tectonic erosion and subduction. *Tectonophysics*, *662*, 454-471.

Safonova, I. (2017). Juvenile versus recycled crust in the Central Asian Orogenic Belt: Implications from ocean plate stratigraphy, blueschist belts and intra-oceanic arcs. *Gondwana Research*, *47*, 6-27.

Safonova, I., Perfilova, A., Obut, O., Kotler, P., Aoki, S., Komiya, T., Wang, B., & Sun, M. (2021). Traces of intra-oceanic arcs recorded in sandstones of eastern Kazakhstan: implications from U–Pb detrital zircon ages, geochemistry, and Nd–Hf isotopes. *International Journal of Earth Sciences*, 1-20.

Şengör, A. M. C. (1990). A new model for the late Palaeozoic—Mesozoic tectonic evolution of Iran and implications for Oman. *Geological Society, London, Special Publications*, *49*(1), 797-831.

Shervais, J. W. (1982). Ti-V plots and the petrogenesis of modern and ophiolitic lavas. *Earth and planetary science letters*, *59*(1), 101-118.

Sisson, V. B., Pavlis, T. L., Roeske, S. M., & Thorkelson, D. J. (2003). Introduction: An overview of ridge-trench interactions in modern and ancient settings. *Geological Society of America Special Papers*, *371*, 1-18.

Sláma, J., Košler, J., Condon, D. J., Crowley, J. L., Gerdes, A., Hanchar, J. M., & Whitehouse, M. J. (2008). Plešovice zircon—a new natural reference material for U–Pb and Hf isotopic microanalysis. *Chemical Geology*, *249*(1-2), 1-35.

Smith, E. I., Sanchez, A., Walker, J. D., & Wang, K. (1999). Geochemistry of mafic magmas in the Hurricane Volcanic field, Utah: implications for small-and large-scale chemical variability of the lithospheric mantle. *The Journal of geology*, *107*(4), 433-448.

Söderlund, U., Patchett, P. J., Vervoort, J. D., & Isachsen, C. E. (2004). The 176Lu decay constant determined by Lu–Hf and U–Pb isotope systematics of Precambrian mafic intrusions. *Earth and Planetary Science Letters*, *219*(3-4), 311-324.

Sorokin, A. A., Zaika, V. A., Kovach, V. P., Kotov, A. B., Xu, W., & Yang, H. (2020). Timing of closure of the eastern Mongol–Okhotsk Ocean: Constraints from U–Pb and Hf isotopic data of detrital zircons from metasediments along the Dzhagdy Transect. *Gondwana Research*, *81*, 58-78.

Sun, S. S., & McDonough, W. F. (1989). Chemical and isotopic systematics of oceanic basalts: implications for mantle composition and processes. *Geological Society, London, Special Publications*, *42*(1), 313-345.

Tang, G. J., Wang, Q., Wyman, D. A., Li, Z. X., Zhao, Z. H., & Yang, Y. H. (2012). Late Carboniferous high εNd (t)–εHf (t) granitoids, enclaves and dikes in western Junggar, NW China: ridge-subduction-related magmatism and crustal growth. *Lithos*, *140*, 86-102.

Taylor, S. R., & McLennan, S. M. (1985). The continental crust: its composition and evolution.

Thorkelson, D. J. (1996). Subduction of diverging plates and the principles of slab window formation. *Tectonophysics*, *255*(1-2), 47-63.

Tomurtogoo, O., Windley, B. F., Kröner, A., Badarch, G., & Liu, D. Y. (2005). Zircon age and occurrence of the Adaatsag ophiolite and Muron shear zone, central Mongolia: constraints on the evolution of the Mongol–Okhotsk ocean, suture and orogen. *Journal of the Geological Society*, *162*(1), 125-134.

Tomurtogoo, O., Byamba, J., Badarch, G., Minjin, C., Orolmaa, D., Khosbayar, P., & Bat-Ireedui, T. (1998). Geological map of Mongolia. scale 1: 1 000 000. *Mineral Resources Authority of Mongolia and Mongolian Academy of Sciences, Ulaanbaatar*.

Vermeesch, P. (2018). IsoplotR: A free and open toolbox for geochronology. *Geoscience Frontiers*, *9*(5), 1479-1493.

Wiedenbeck, M., Hanchar, J. M., Peck, W. H., Sylvester, P., Valley, J., Whitehouse, M., ... & Zheng, Y. F. (2004). Further characterisation of the 91500 zircon crystal. *Geostandards and Geoanalytical Research*, *28*(1), 9-39.

Windley, B. F., Alexeiev, D., Xiao, W., Kröner, A., & Badarch, G. (2007). Tectonic models for accretion of the Central Asian Orogenic Belt. *Journal of the Geological Society*, *164*(1), 31-47.

Windley, B. F., & Xiao, W. (2018). Ridge subduction and slab windows in the Central Asian Orogenic Belt: Tectonic implications for the evolution of an accretionary orogen. *Gondwana Research*, *61*, 73-87.

Winkler, W., Bussien, D., Baatar, M., Anaad, C., & von Quadt, A. (2020). Detrital zircon provenance analysis in the central Asian orogenic belt of central and southeastern Mongolia—A Palaeotectonic model for the Mongolian Collage. *Minerals*, *10*(10), 880.

Wilhem, C., Windley, B. F., & Stampfli, G. M. (2012). The Altaids of Central Asia: a tectonic and evolutionary innovative review. *Earth-Science Reviews*, *113*(3-4), 303-341.

Wilson, B. M. (2007). *Igneous petrogenesis a global tectonic approach*. Springer Science & Business Media.

Wu, F. Y., Sun, D. Y., Ge, W. C., Zhang, Y. B., Grant, M. L., Wilde, S. A., & Jahn, B. M. (2011). Geochronology of the Phanerozoic granitoids in northeastern China. *Journal of Asian Earth Sciences*, *41*(1), 1-30.

Xiao, W., Windley, B. F., Hao, J., & Zhai, M. (2003). Accretion leading to collision and the Permian Solonker suture, Inner Mongolia, China: Termination of the central Asian orogenic belt. *Tectonics*, *22*(6).

Yakubchuk, A. (2017). Evolution of the Central Asian Orogenic Supercollage since late Neoproterozoic revised again. *Gondwana Research*, *47*, 372-398.

Yakymchuk, C., Kirkland, C. L., & Clark, C. (2018). Th/U ratios in metamorphic zircon. *Journal of Metamorphic Geology*, *36*(6), 715-737.

Zaytsev, N. S. & Luchitsky, I.V. (1979). Geology and magmatism of Mongolia, The Joint Soviet-Mongolian Scientific-Research Geological Expedition, Transactions, vol. 30, Nauka, Moscow.

Zhang, H., Harris, N., Parrish, R., Kelley, S., Zhang, L., Rogers, N., & King, J. (2004). Causes and consequences of protracted melting of the mid-crust exposed in the North Himalayan antiform. *Earth and Planetary Science Letters*, *228*(1-2), 195-212.

Zhao, J. H., & Zhou, M. F. (2009). Secular evolution of the Neoproterozoic lithospheric mantle underneath the northern margin of the Yangtze Block, South China. *Lithos*, *107*(3-4), 152-168.

Zhao, P., Appel, E., Xu, B., & Sukhbaatar, T. (2020). First paleomagnetic result from the Early Permian volcanic rocks in northeastern Mongolia: Evolutional implication for the Paleo-Asian Ocean and the Mongol-Okhotsk Ocean. *Journal of Geophysical Research: Solid Earth*, *125*(2), e2019JB017338.

Zhao, P., Xu, B., & Jahn, B. M. (2017). The Mongol-Okhotsk Ocean subduction-related Permian peraluminous granites in northeastern Mongolia: Constraints from zircon U-Pb ages, whole-rock elemental and Sr-Nd-Hf isotopic compositions. *Journal of Asian Earth Sciences*, *144*, 225-242.

Zhu, M., Zhang, F., Miao, L., Baatar, M., Anaad, C., Yang, S., & Li, X. (2016). Geochronology and geochemistry of the Triassic bimodal volcanic rocks and coeval A-type granites of the Olzit area, Middle Mongolia: Implications for the tectonic evolution of Mongol–Okhotsk Ocean. *Journal of Asian Earth Sciences*, *122*, 41-57.

Zhu, M. S., Zhang, F., Miao, L. C., Baatar, M., Anaad, C., Yang, S. H., & Li, X. B. (2018). The late Carboniferous khuhu davaa ophiolite in northeastern Mongolia: Implications for the tectonic evolution of the Mongol–Okhotsk ocean. *Geological Journal*, *53*(4), 1263-1278.

Zonenshain, L. P., Kuzmin, M. I., Natapov, L. M., & Page, B. M. (1990). Mongol-Okhotsk Foldbelt. *Geology of the USSR: A Plate-Tectonic Synthesis*, *21*, 97-108.

Zorin, Y. A., Belichenko, V. G., Turutanov, E. K., Kozhevnikov, V. M., Ruzhentsev, S. V., Dergunov, A. B., & Khosbayar, P. (1993). The south Siberia-central Mongolia transect. *Tectonophysics*, *225*(4), 361-378.

Zorin, Y. A. (1999). Geodynamics of the western part of the Mongolia–Okhotsk collisional belt, Trans-Baikal region (Russia) and Mongolia. *Tectonophysics*, *306*(1), 33-56.

CAPTIONS

Figure 1. Sketch map illustrating the major tectonic units along the Mongol-Okhotsk Belt (Modified after Zorin, 1999; Khanchuk et al., 2015; Miao et al., 2020). Inset map showing the location of the CAOB (Modified after Safonova et al., 2017).

Figure 2. Simplified geological map of the Middle Gobi Belt (modified after the 1:200 000 State Geological Map), showing sample locations.

Figure 3. Representative field photos of the Mandalgovi pluton

Figure 4. Photomicrographs of cross-polarized light view showing textures and mineral assemblage of the studied samples from the Middle Mandalgovi pluton, Middle Gobi Belt. (a, b) Gabbrodiorite (Sample D0909); (c, d) Biotite-granite (sample D0906); (e, f) Granodiorite (sample D0914); Bt—biotite; Hbl—hornblende; Kfs—K-feldspar; Pl—plagioclase; Qz—quartz.

Figure 5. Major element discrimination diagrams showing the compositions and characteristics of the studied samples from Middle Gobi Belt. (a) SiO_2 versus (Na_2O + K_2O) total alkali-silica (TAS) diagram for plutonic rocks (after Irvine and Baragar, 1971), (b) SiO_2 versus (Na_2O + K_2O) total alkali-silica (TAS) diagram for volcanic rocks (after Le Bas et al., 1986), (c) K_2O wt% versus SiO_2 wt% plot (Peccerillo and Taylor, 1976), (d) A/CNK [molar $Al_2O_3/(CaO \times Na_2O \times K_2O)$] versus A/NK [molar $Al_2O_3/(Na_2O \times K_2O)$] diagram, the boundary line is from Maniar and Piccoli (1989).

Figure 6. CI-chondrite-normalized REE patterns and primitive-mantle-normalized trace element spidergrams for the studied samples from the Middle Gobi Belt. Both chondrite and primitive-mantle normalized values are from Sun and McDonough (1989). Green shaded area show island arc derived rocks, pink shaded area shows active continental margin. Data from GEOROC. (http://www.earthchem.org/).

Figure 7. Cathodoluminescence (CL) images of representative zircon crystals from the studied samples from the Middle Gobi Belt. White circles show individual analysis spots, corresponding Pb–Pb ages and red circles show an individual spot of Lu-Hf isotope and their $\varepsilon_{Hf}(t)$ values.

Figure 8. Concordia diagrams of zircons for samples from the Middle Gobi Belt, showing U-Pb isotope ratios. Light grayish ellipses indicates discordant data excluded from the calculation.

Figure 9. (a) Ba versus Sr diagram, (b) Sr versus Eu diagram showing mineral fractionation.

Figure 10. (a) CaO/Al_2O_3 versus $CaO + Al_2O_3$ wt% plot; (b) The Ab–Or–Qz normative diagram of the of the studied samples from Middle Gobi Belt. Solidus curves from Manning (1981).

Figure 11. (a) $(Na_2O+K_2O)/(FeO^T+TiO2)$ versus $Na_2O+K_2O+FeO^T+MgO+TiO_2$, wt% diagram, (b) molar $Al_2O_3/(Mg+FeO^T)$ versus molar $CaO/(MgO+FeO^T)$ for source determination, (c) Plots of Rb/Ba versus Rb/Sr, (d) CaO/Na_2O versus Al_2O_3/TiO_2 plots for source characteristics (Patiño Douce and Johnston, 1991; Patiño Douce and Harris, 1998).

Figure 12. Correlations between whole-rock $\varepsilon_{Nd}(t)$ and zircon concordant ages. (b) Correlations between $\varepsilon_{Hf}(t)$ and U–Pb ages of zircons for the studied samples from the Middle Gobi Belt. Compared data from Zhu et al., 2016; Zhao et al., 2017.

Figure 13. (a) $MgO–Al_2O_3–FeO^T$ ternary diagram for tectonic discrimination of mafic rocks from the Middle Gobi Belt (Pearce et al. 1977); (b) Ba versus Zr tectonic discrimination diagram of mafic rocks from the Middle Gobi Belt (Shervais, 1982).

Table 1. Major (wt%) and trace (µg/g) element compositions including sample location and rock type of the studied samples from the Middle Gobi Belt.

Table 2. LA-ICPMS U–Th–Pb analytical data for zircons of the studied samples from the Middle Gobi Belt. * Discordant data excluded from calculation.

Table 3. Zircon Lu-Hf and whole-rock Sm-Nd isotope data of the studied samples from the Middle Gobi

Fig. 1

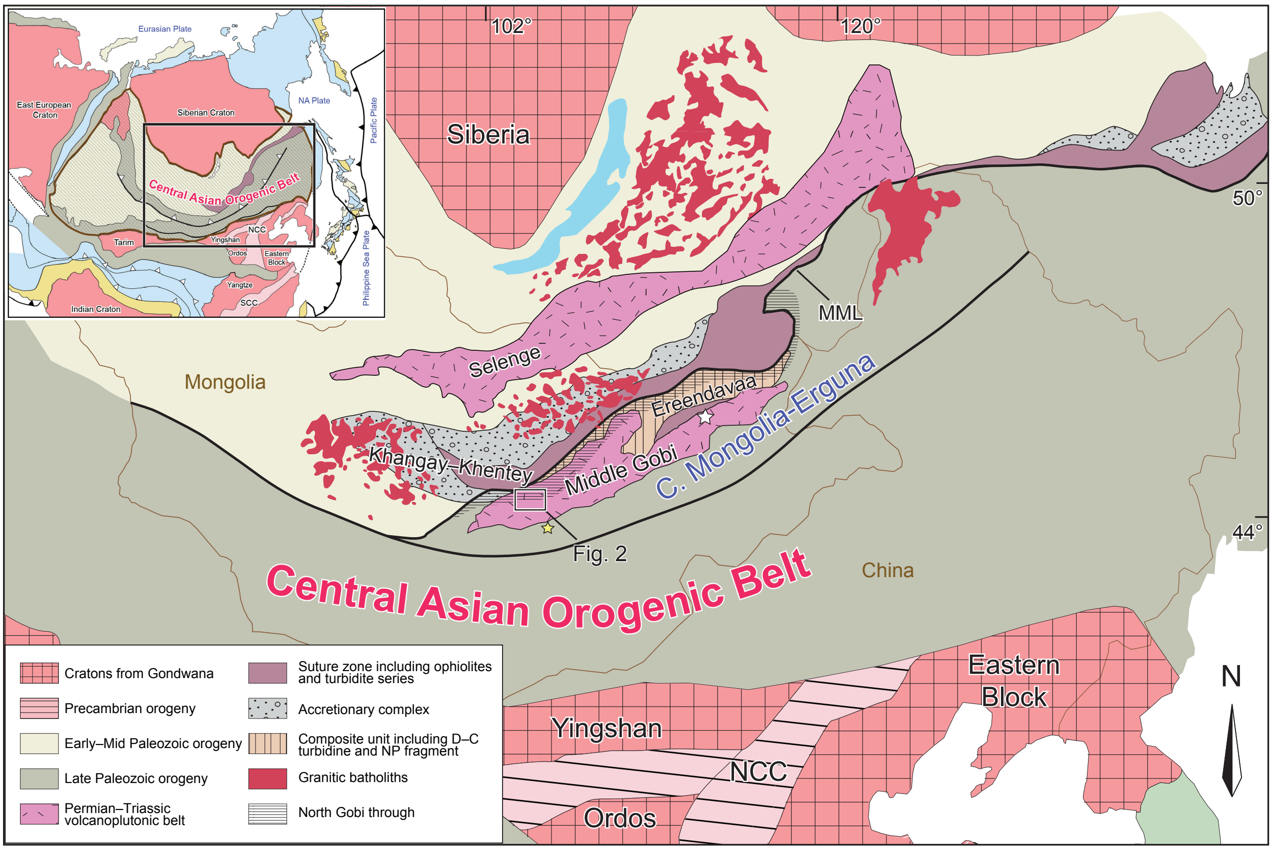
Eurasian Plate
East European Craton
Siberian Craton
NA Plate
Pacific Plate
Central Asian Orogenic Belt
Tarim
Yingshan
NCC
Ordos
Eastern Block
Yangtze
SCC
Indian Craton
Philippine Sea Plate
102°
120°
Siberia
50°
44°
Selenge
MML
Mongolia
Ereendavaa
C. Mongolia-Erguna
Khangay-Khentey
Middle Gobi
Fig. 2
Central Asian Orogenic Belt
China
Eastern Block
Yingshan
NCC
Ordos
N
Cratons from Gondwana
Precambrian orogeny
Early–Mid Paleozoic orogeny
Late Paleozoic orogeny
Permian–Triassic volcanoplutonic belt
Suture zone including ophiolites and turbidite series
Accretionary complex
Composite unit including D–C turbidine and NP fragment
Granitic batholiths
North Gobi through

Fig. 2

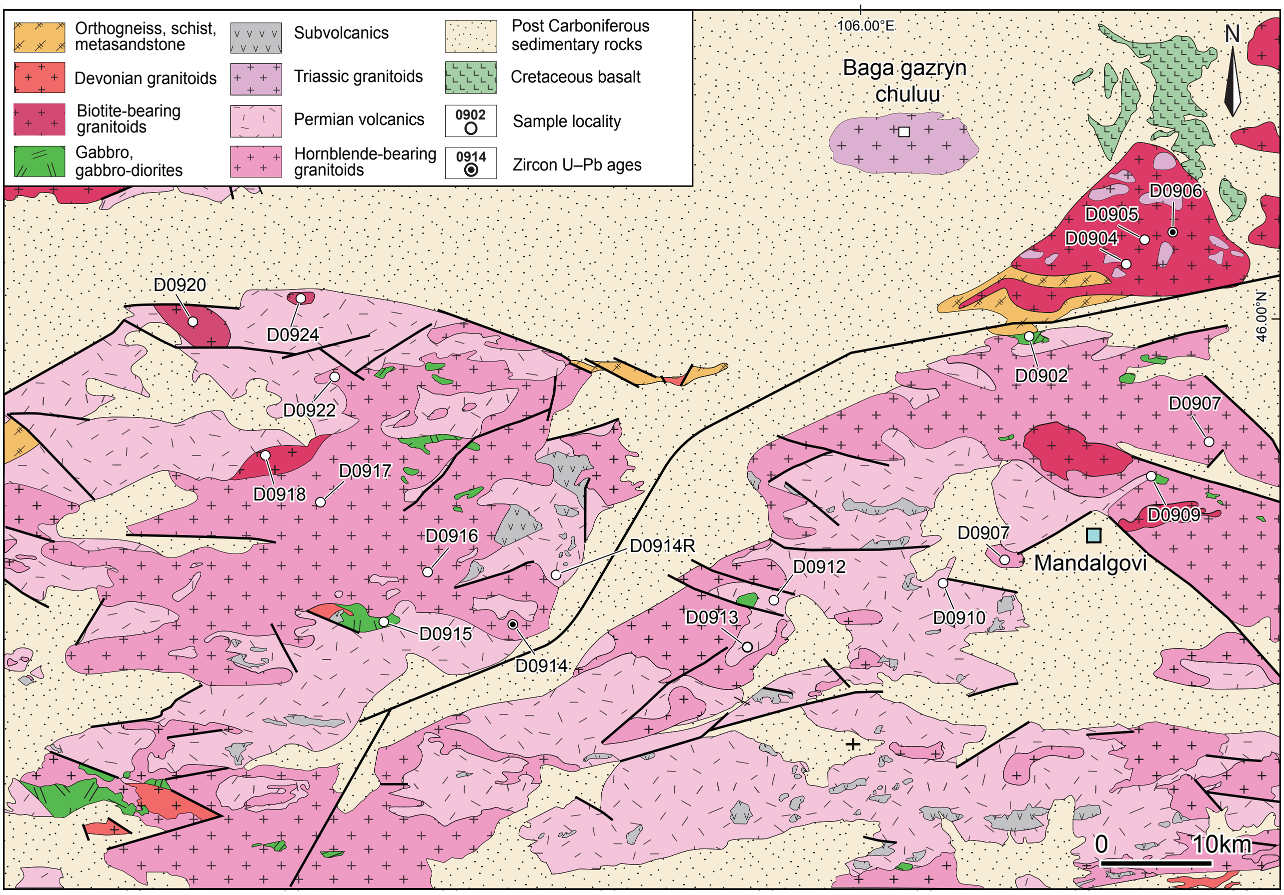
Orthogneiss, schist, metasandstone
Devonian granitoids
Biotite-bearing granitoids
Gabbro, gabbro-diorites
Subvolcanics
Triassic granitoids
Permian volcanics
Hornblende-bearing granitoids
Post Carboniferous sedimentary rocks
Cretaceous basalt
0902 Sample locality
0914 Zircon U–Pb ages
106.00°E
46.00°N
N
Baga gazryn chuluu
Mandalgovi
D0920
D0924
D0922
D0918
D0917
D0916
D0915
D0914
D0914R
D0913
D0912
D0910
D0907
D0909
D0902
D0904
D0905
D0906
0
10km

Fig. 3

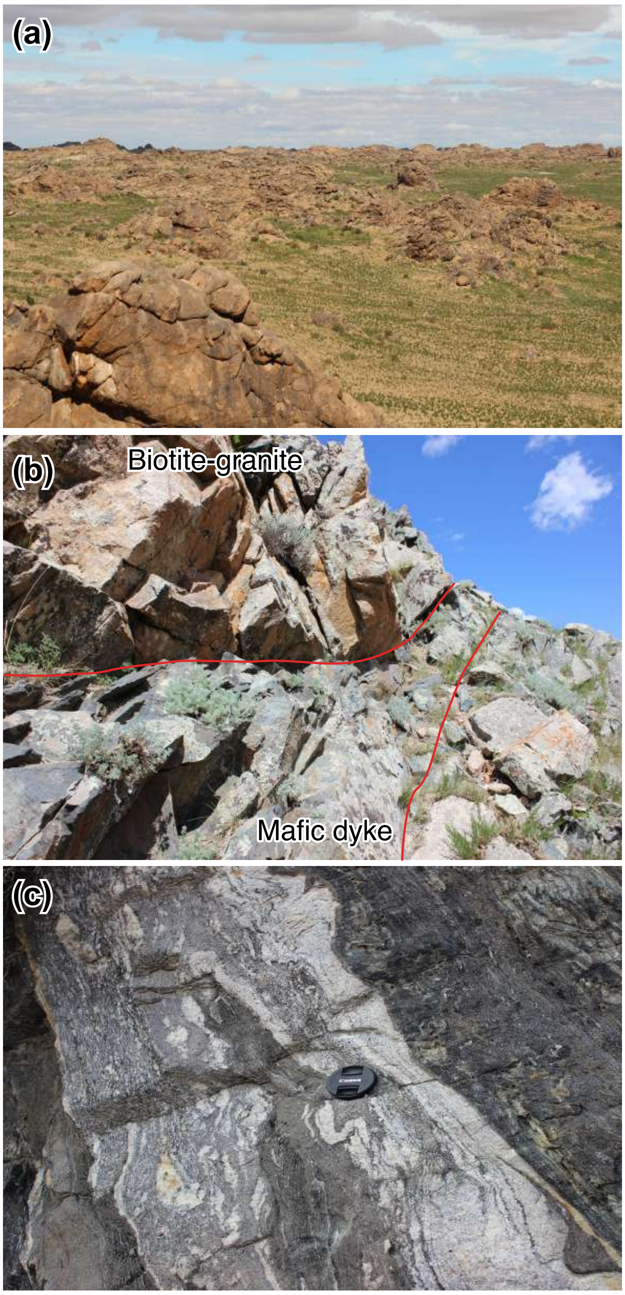

Fig. 4

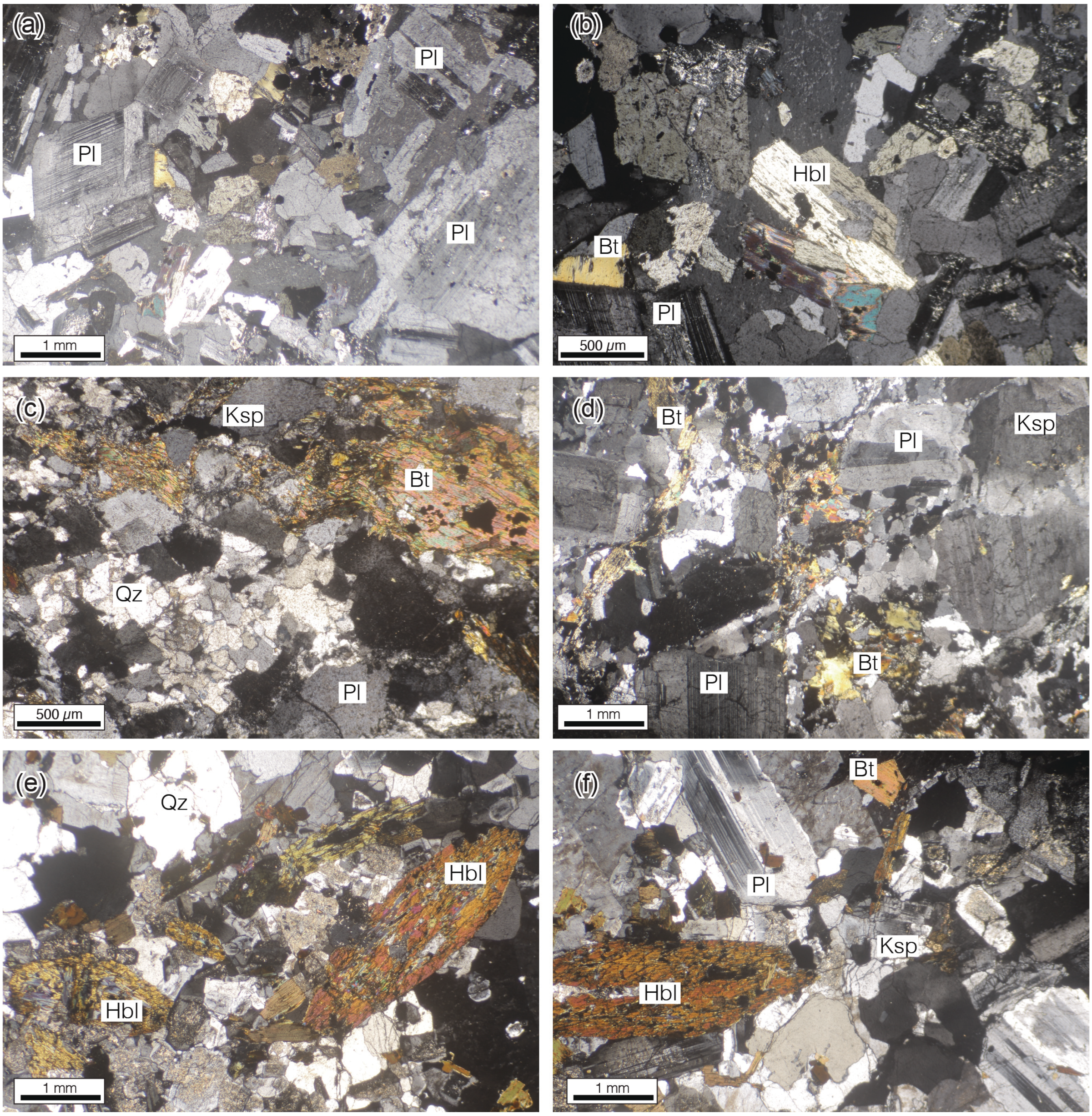
(a)
Pl
Pl
Pl
1 mm
(b)
Hbl
Bt
Pl
500 μm
(c)
Ksp
Bt
Qz
Pl
500 μm
(d)
Bt
Pl
Ksp
Pl
Bt
1 mm
(e)
Qz
Hbl
Hbl
1 mm
(f)
Bt
Pl
Ksp
Hbl
1 mm

Fig. 5

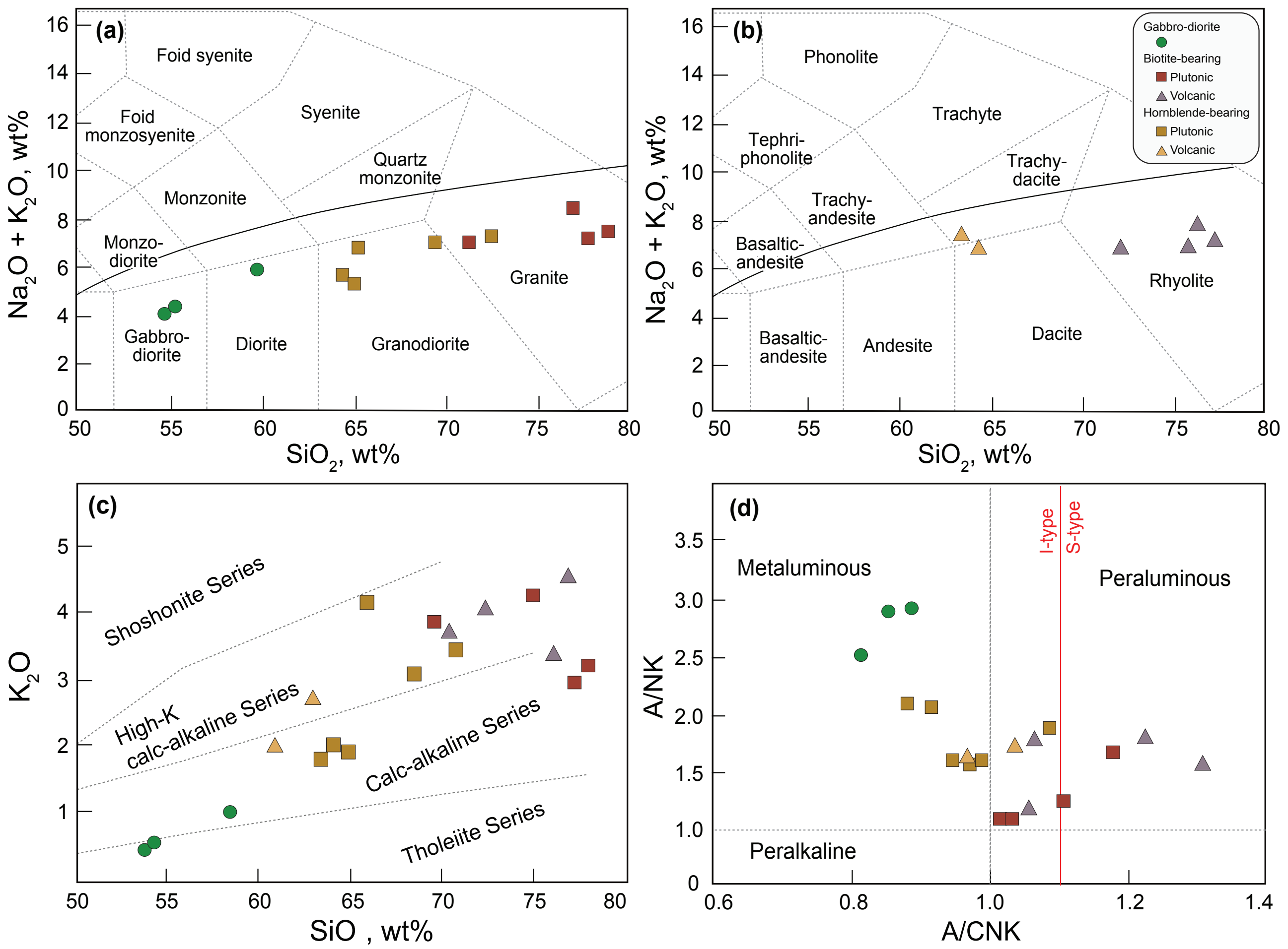
(a)
Foid syenite
Foid monzosyenite
Syenite
Quartz monzonite
Monzonite
Monzo-diorite
Gabbro-diorite
Diorite
Granodiorite
Granite
Na2O + K2O, wt%
SiO2, wt%
(b)
Phonolite
Tephri-phonolite
Trachyte
Trachy-dacite
Trachy-andesite
Basaltic-andesite
Basaltic-andesite
Andesite
Dacite
Rhyolite
Gabbro-diorite
Biotite-bearing
Plutonic
Volcanic
Hornblende-bearing
Plutonic
Volcanic
(c)
Shoshonite Series
High-K calc-alkaline Series
Calc-alkaline Series
Tholeiite Series
K2O
SiO , wt%
(d)
Metaluminous
Peraluminous
Peralkaline
I-type
S-type
A/NK
A/CNK

Fig. 6

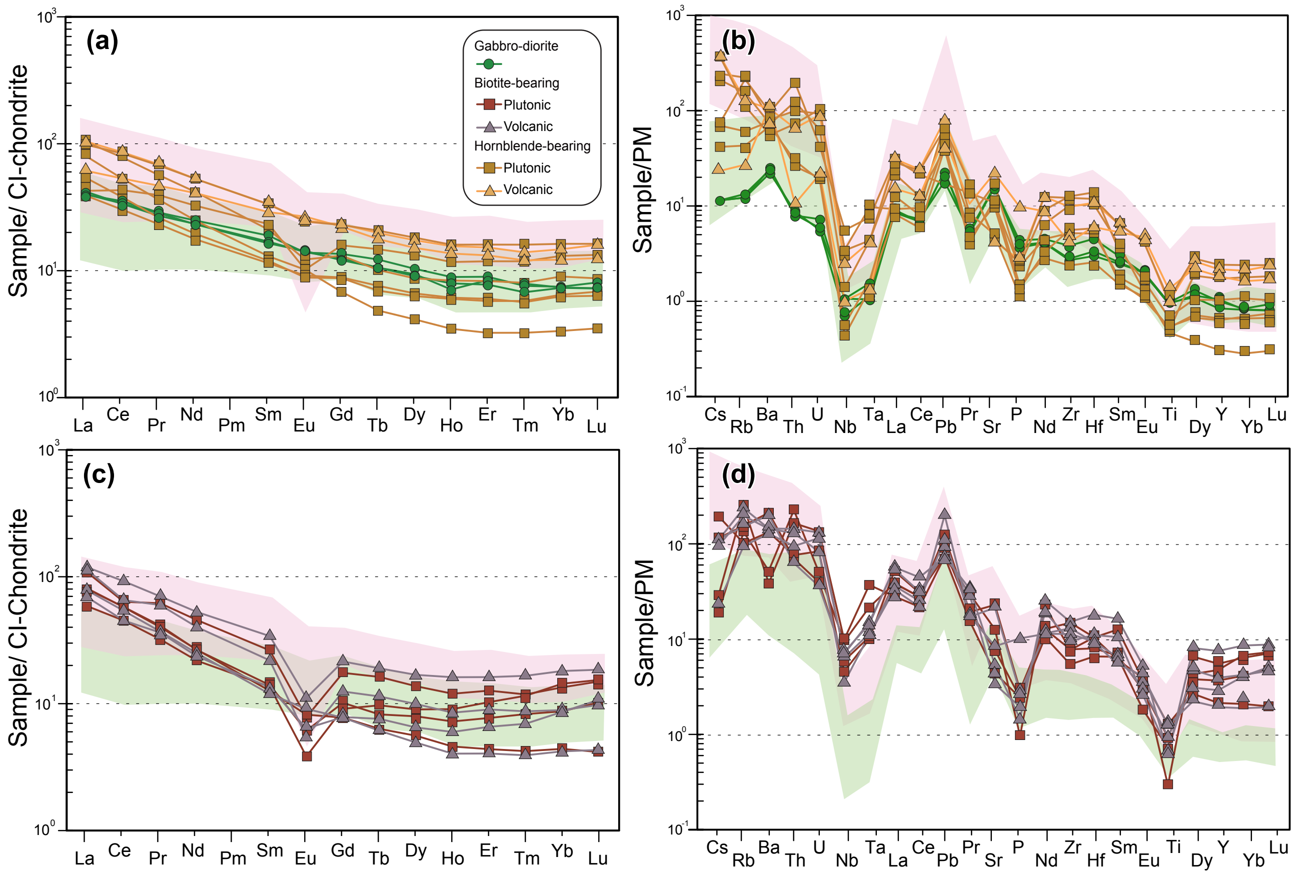

(a)
Sample/ CI-chondrite
Gabbro-diorite
Biotite-bearing
Plutonic
Volcanic
Hornblende-bearing
Plutonic
Volcanic
La Ce Pr Nd Pm Sm Eu Gd Tb Dy Ho Er Tm Yb Lu
(b)
Sample/PM
Cs Rb Ba Th U Nb Ta La Ce Pb Pr Sr P Nd Zr Hf Sm Eu Ti Dy Y Yb Lu
(c)
Sample/ CI-Chondrite
La Ce Pr Nd Pm Sm Eu Gd Tb Dy Ho Er Tm Yb Lu
(d)
Sample/PM
Cs Rb Ba Th U Nb Ta La Ce Pb Pr Sr P Nd Zr Hf Sm Eu Ti Dy Y Yb Lu

Fig. 7

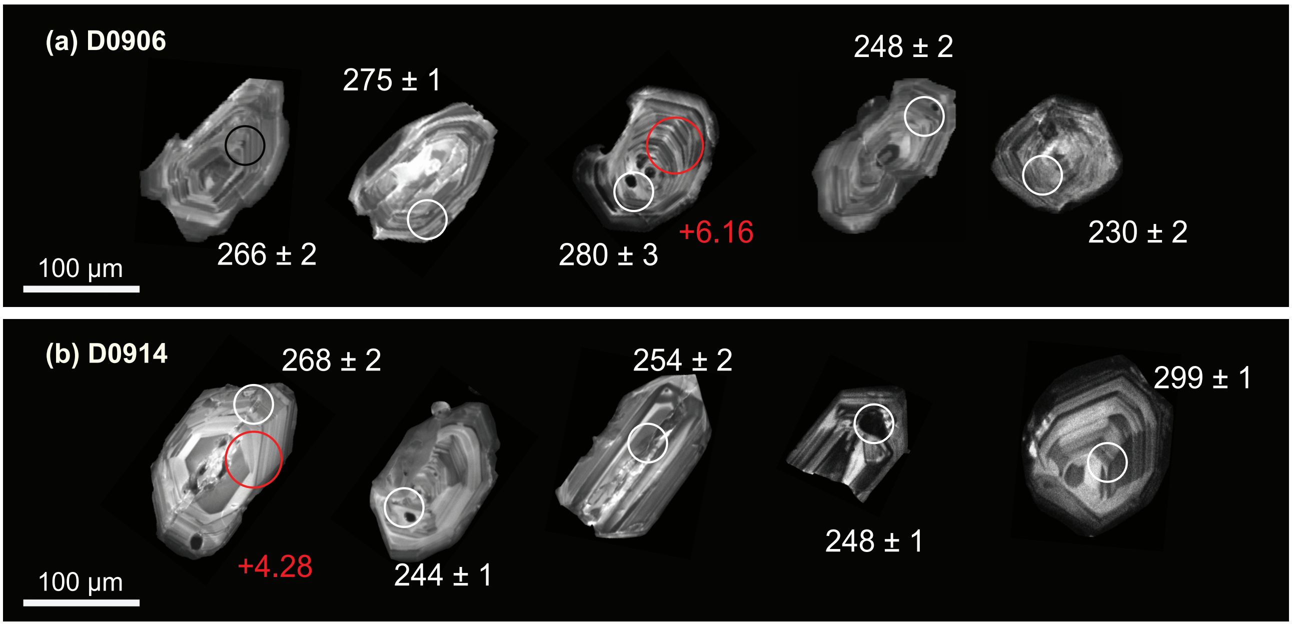

(a) D0906
275 ± 1
248 ± 2
266 ± 2
280 ± 3
+6.16
230 ± 2
100 μm
(b) D0914
268 ± 2
254 ± 2
299 ± 1
+4.28
244 ± 1
248 ± 1
100 μm

Fig. 8

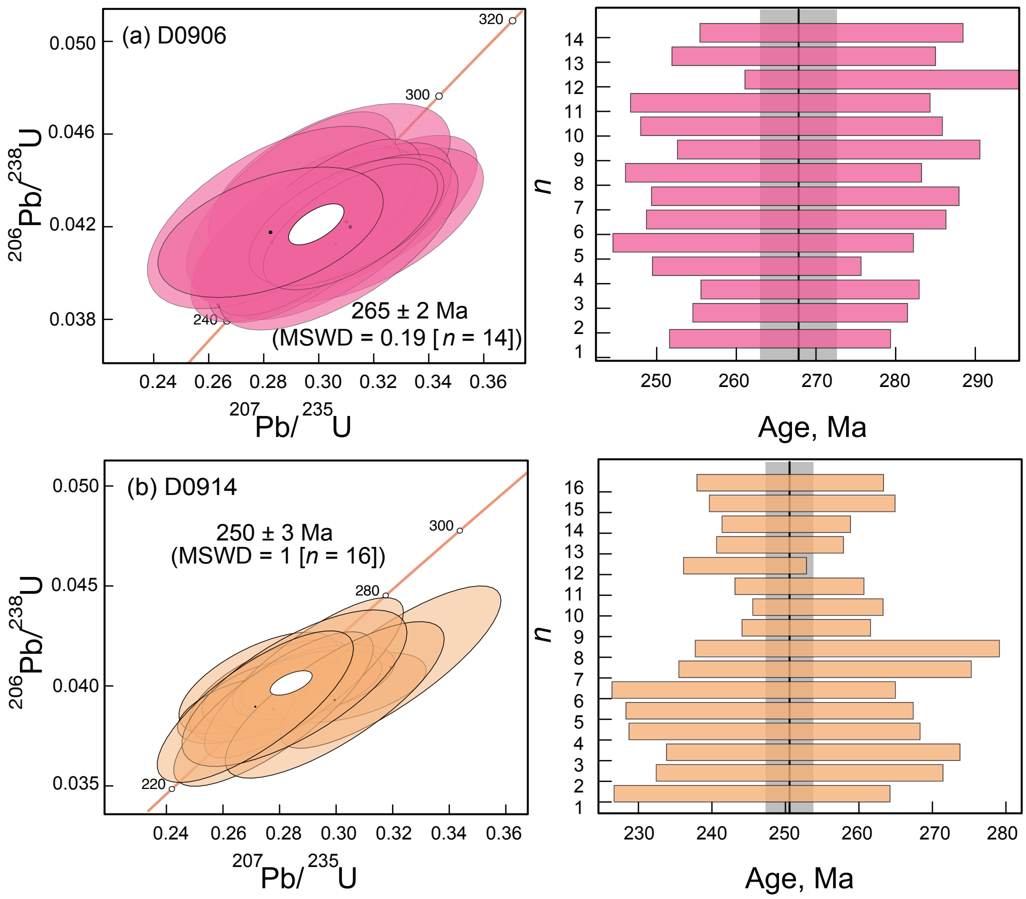

(a) D0906
265 ± 2 Ma
(MSWD = 0.19 [n = 14])
320
300
240
0.050
0.046
0.042
0.038
0.24
0.26
0.28
0.30
0.32
0.34
0.36
206Pb/238U
207Pb/235U
n
Age, Ma
250
260
270
280
290
(b) D0914
250 ± 3 Ma
(MSWD = 1 [n = 16])
300
280
220
0.050
0.045
0.040
0.035
230
240
250
260
270
280

Fig. 9

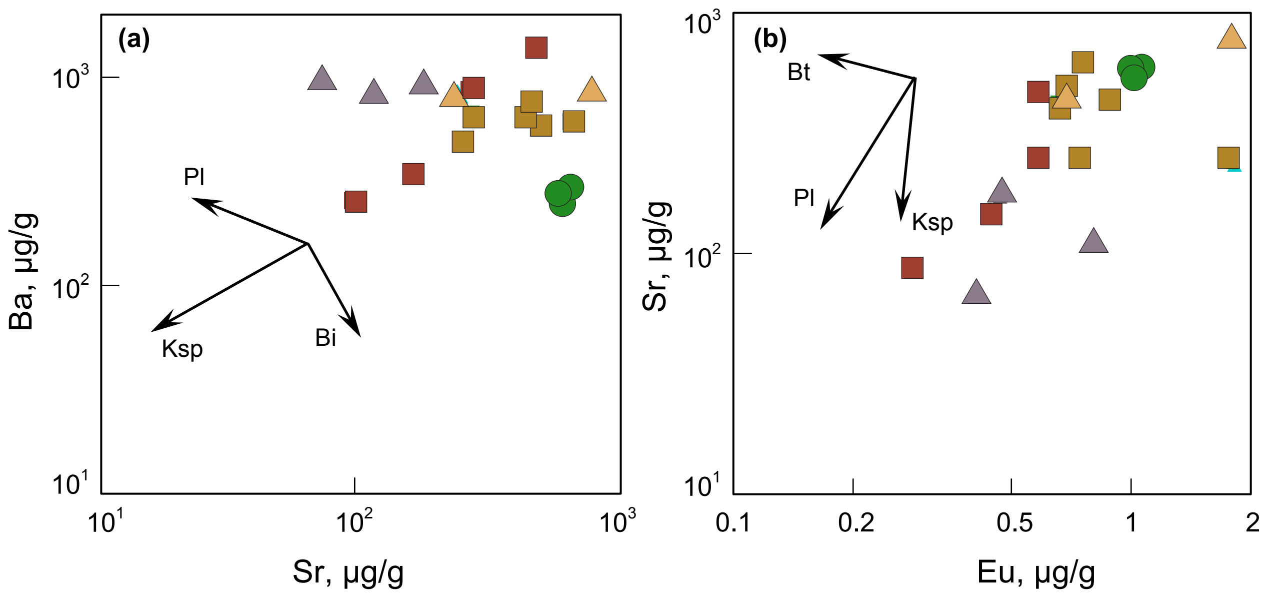

Fig. 10

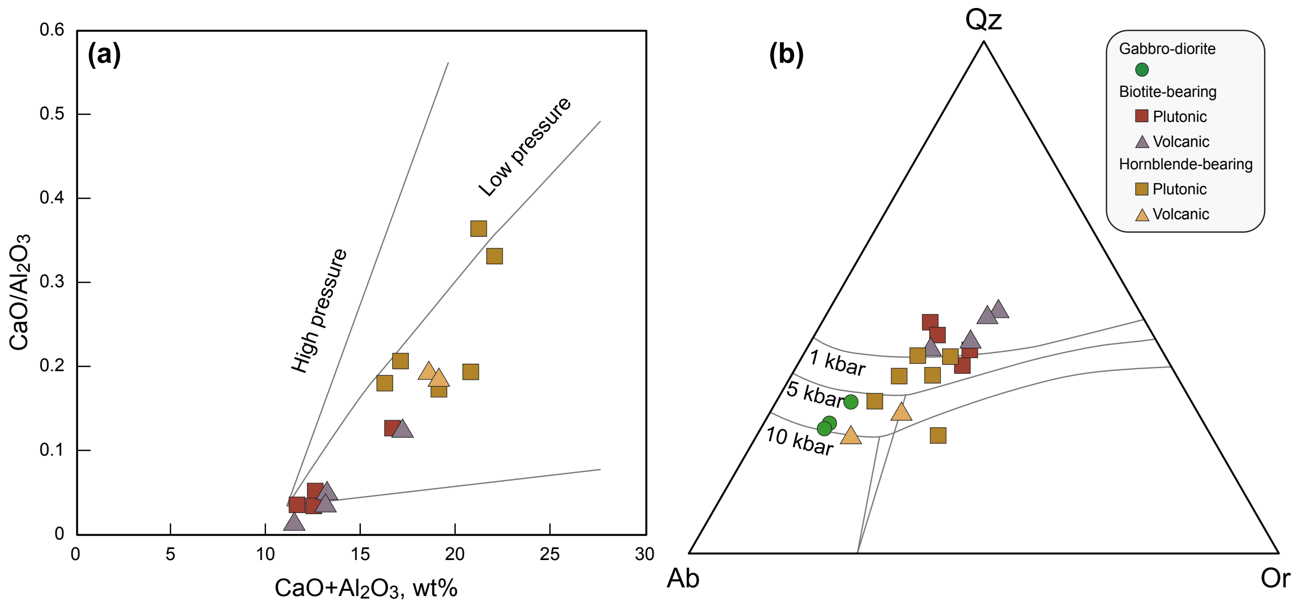

(a)
0.6
0.5
0.4
0.3
0.2
0.1
0
0
5
10
15
20
25
30
CaO/Al2O3
CaO+Al2O3, wt%
High pressure
Low pressure
(b)
Qz
Ab
Or
1 kbar
5 kbar
10 kbar
Gabbro-diorite
Biotite-bearing
Plutonic
Volcanic
Hornblende-bearing
Plutonic
Volcanic

Fig. 11

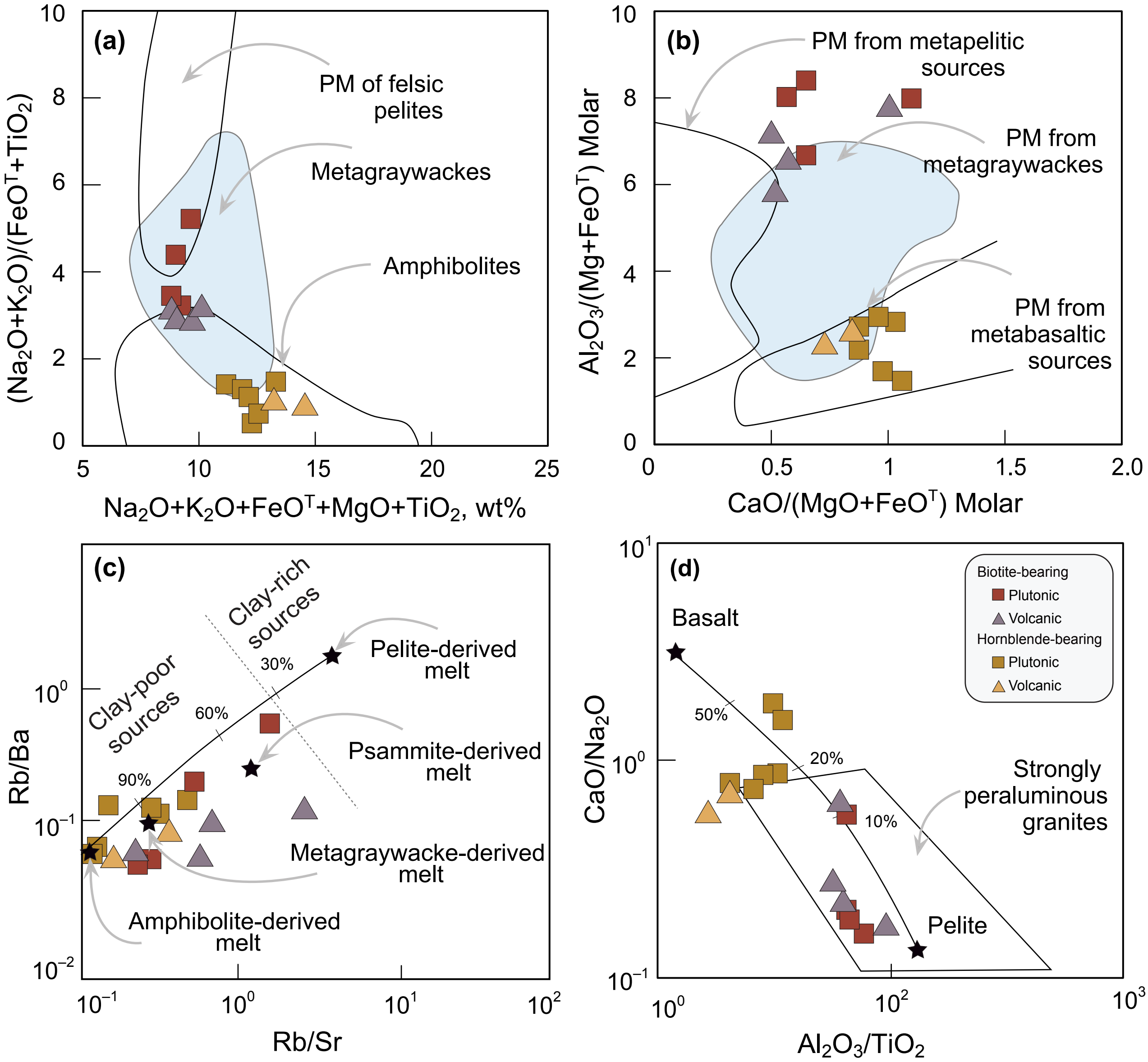

(a)
PM of felsic pelites
Metagraywackes
Amphibolites
(Na2O+K2O)/(FeOT+TiO2)
Na2O+K2O+FeOT+MgO+TiO2, wt%
(b)
PM from metapelitic sources
PM from metagraywackes
PM from metabasaltic sources
Al2O3/(Mg+FeOT) Molar
CaO/(MgO+FeOT) Molar
(c)
Clay-rich sources
Clay-poor sources
30%
60%
90%
Pelite-derived melt
Psammite-derived melt
Metagraywacke-derived melt
Amphibolite-derived melt
Rb/Ba
Rb/Sr
(d)
Basalt
50%
20%
10%
Strongly peraluminous granites
Pelite
Biotite-bearing
Plutonic
Volcanic
Hornblende-bearing
Plutonic
Volcanic
CaO/Na2O
Al2O3/TiO2

Fig. 12

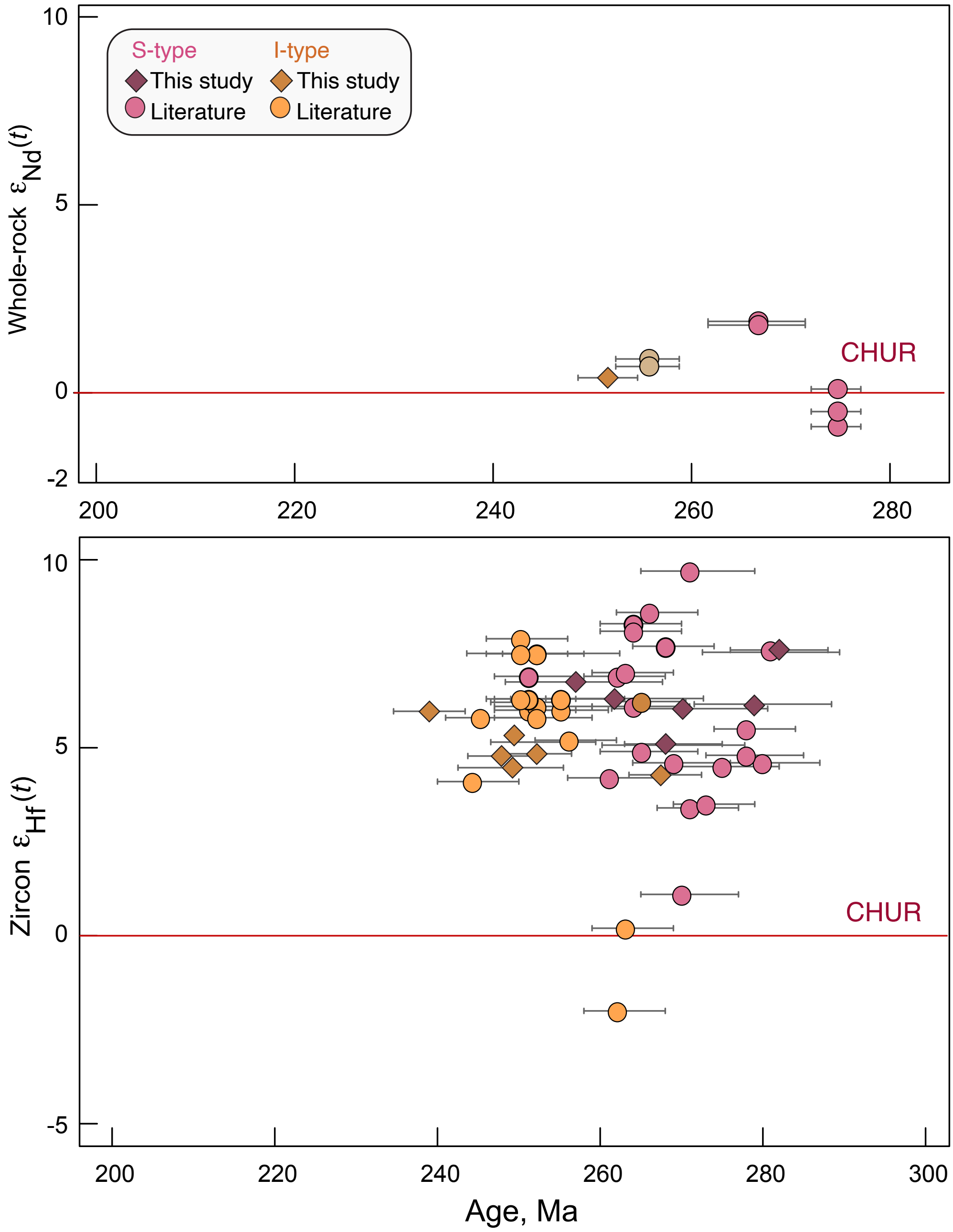

S-type
This study
Literature
I-type
This study
Literature
Whole-rock $\varepsilon_{Nd}(t)$
CHUR
10
5
0
-2
200
220
240
260
280
Zircon $\varepsilon_{Hf}(t)$
CHUR
10
5
0
-5
200
220
240
260
280
300
Age, Ma

Fig. 13

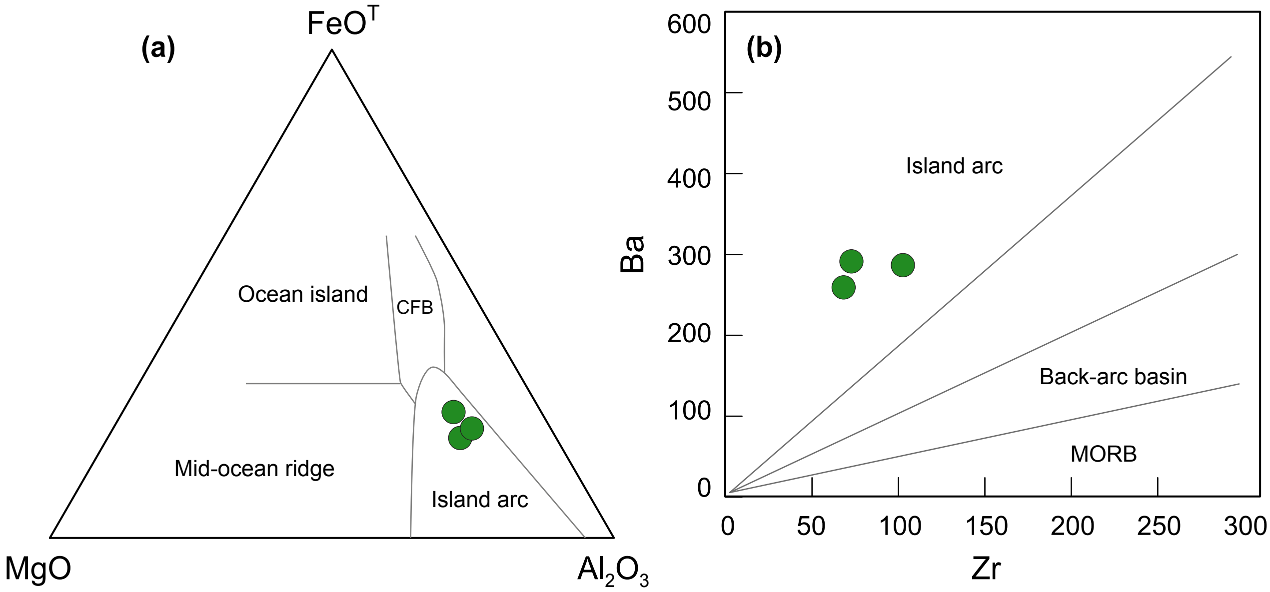

(a)
FeO^T
Ocean island
CFB
Mid-ocean ridge
Island arc
MgO
Al2O3
(b)
600
500
400
300
200
100
0
Ba
Island arc
Back-arc basin
MORB
0
50
100
150
200
250
300
Zr

Table 1

Sample	D0902	D0904	D0905	D0907	D0909	D0910	D80914	D0915	D0917	D0920	D0912	D0913	D0909-2	D0914-R	D0918-1	D0918-2	D0922-1	D0922-2	D0924
SiO_2	54.06	77.39	74.75	70.75	63.01	72.53	65.23	58.74	68.59	63.53	61.1	76.93	54.12	76.22	69.82	70.48	64.19	64.83	0.059
TiO_2	0.792	0.188	0.146	0.471	0.796	0.191	0.61	0.774	0.464	0.506	1.006	0.136	0.793	0.124	0.255	0.264	0.514	0.834	11.25
Al_2O_3	18.52	12	12.13	13.77	16.15	12.68	16.14	16.24	14.11	16	15.69	11.44	17.67	12.38	15.05	15.31	15.32	17.36	1.69
FeO	8.19	1.84	1.42	3.43	5.48	2.27	4.25	6.78	4.09	4.95	6.76	2.67	8.78	2.46	1.69	1.75	5.12	4.79	1.52
MnO	0.128	0.035	0.024	0.055	0.104	0.029	0.09	0.16	0.045	0.085	0.126	0.024	0.138	0.028	0.023	0.028	0.083	0.107	0.036
MgO	4.08	0.25	0.17	1.16	1.18	0.1	1.15	2.89	1.37	2.59	1.14	0.09	4.34	0.13	0.31	0.32	2.57	1.19	0.08
CaO	8.05	0.6	0.45	2.49	2.97	0.44	2.93	5.75	2.93	5.31	2.97	0.1	8.51	0.57	1.88	1.88	5.49	3.36	0.4
Na_2O	3.26	3.98	3.89	3.44	4.33	2.72	4.22	3.98	3.79	3.45	5.22	2.62	3.15	4.31	3.14	3.06	3.09	4.64	4.08
K_2O	0.77	2.99	4.32	3.44	2.77	4.07	3.99	2.79	3.07	1.91	2.02	4.53	0.79	3.36	3.85	3.72	2.06	2.01	3.25
P_2O_5	0.21	0.05	0.05	0.09	0.17	0.21	0.15	0.15	0.15	0.11	0.44	0.04	0.24	0.03	0.06	0.06	0.1	0.16	0.02
LOI	2.42	1.43	1.23	1.47	1.36	3.4	1.02	2.42	1.22	1.62	3.99	2.02	2.25	0.72	3.61	3.5	1.61	1.52	1.28
Total	100.5	100.8	98.58	100.6	98.33	98.64	99.94	100.7	99.81	100.1	100.4	100.6	100.8	100.3	99.7	100.4	100.2	100.8	100.1
Rb	15	80	150	128	85	118	124	105	98	38	27	142	16	57	93	93	49	77	61
Sr	611	153	88	258	228	168	455	642	635	478	779	67	591	107	455	440	427	238	253
Y	15.3	15.8	20.4	26	30.8	12.5	17.8	25.6	7.3	12.8	27.2	16.9	17.4	32.3	9.2	8.8	12.4	33.4	23.7
Cs	0.5	0.4	0.6	4.8	6.6	2	2	1.9	4.3	1.3	1.2	2.3	0.5	0.5	2.4	2.4	1.9	6.5	4.1
Ba	256	344	255	665	804	948	759	484	614	592	852	955	271	844	1400	1339	643	505	875
La	12.4	24.8	18.2	13.2	32.3	21.4	32	36.2	24.8	12.1	19	35.1	12.3	36.8	25.1	24.2	16.7	30.5	33.6
Ce	27.3	46.7	36.5	34.8	69.2	36.5	63	76.6	42.8	24.4	43	52.8	28.5	74.5	46.5	43.6	30.6	67.6	51.3
Pr	3.46	5.02	3.92	4.8	8.38	4.43	6.9	8.68	4.41	2.83	5.69	7.31	3.5	8.54	4.89	4.52	3.18	8.22	7.54
Nd	13.9	15.9	13.1	19.5	31.7	14.2	25	30.6	14.9	10.6	24.5	24.1	14.9	31.7	16	15	11.7	31.7	27.4
Sm	3.2	2.73	2.65	4.54	6.51	2.62	4.1	5.93	2.53	2.23	5.64	4.27	3.68	6.64	2.46	2.32	2.33	6.49	5.12
Eu	1.05	0.45	0.282	0.75	1.82	0.468	0.9	1.03	0.748	0.673	1.96	0.402	1.02	0.815	0.602	0.668	0.649	1.79	0.575
Gd	3.13	2.63	2.36	4.1	5.99	2.03	3.4	4.84	1.76	2.29	5.76	3.23	3.51	5.57	2.01	2.01	2.26	5.94	4.53
Tb	0.5	0.39	0.46	0.7	0.94	0.36	0.48	0.78	0.23	0.36	0.84	0.54	0.58	0.9	0.3	0.29	0.33	0.98	0.77
Dy	2.92	2.56	2.9	4.31	5.59	2.09	2.8	4.67	1.33	2.13	4.87	3.2	3.33	5.43	1.8	1.59	2.03	5.86	4.42
Ho	0.57	0.52	0.65	0.84	1.12	0.43	0.6	0.92	0.25	0.44	0.98	0.61	0.64	1.16	0.33	0.29	0.43	1.15	0.86
Er	1.63	1.62	2.16	2.49	3.2	1.38	1.74	2.61	0.68	1.26	2.77	1.89	1.88	3.4	0.92	0.85	1.21	3.37	2.66
Tm	0.219	0.268	0.374	0.384	0.452	0.225	0.26	0.415	0.105	0.183	0.391	0.282	0.246	0.537	0.137	0.127	0.187	0.519	0.383
Yb	1.53	1.82	3	2.73	3.08	1.8	1.88	2.85	0.7	1.31	2.55	1.86	1.56	3.78	0.92	0.88	1.35	3.4	2.81
Lu	0.233	0.329	0.495	0.429	0.515	0.345	0.28	0.419	0.113	0.204	0.404	0.315	0.26	0.596	0.134	0.139	0.22	0.524	0.481
Pb	6	13	11	14	15	30		18	9	9	11	12	5	11	18	17	10	13	11
Th	1.56	18.1	13.2	9.42	6.91	10.4	15.7	13.6	11.1	3.87	1.79	11.5	1.45	7.58	5.59	5.16	3.49	7.46	6.1
U	0.28	1	2.71	2.24	2.19	1.65	1.25	1.75	1.68	0.68	0.76	2.63	0.34	2.3	0.79	0.74	0.71	2.43	1.67
Zr	73	82	57	227	223	119	268	75	139	70	118	100	111	159	156	142	147	261	81
Nb	2	6.2	6.5	6.5	5.1	2.3	9.2	8.4	3.3	1.4	2.6	4.6	2.7	4.8	3.9	4.4	1.7	6.4	3
Hf	1.9	2.7	2.2	7.1	5.5	3.3	6.4	2.4	3.8	1.9	3.4	3.2	3.1	4.9	3.8	3.9	3.8	6.7	2.7
Ta	0.16	0.8	1.37	0.78	0.42	0.41	0.65	0.6	0.43	0.18	0.18	0.56	0.15	0.53	0.39	0.44	0.21	0.43	0.37
Sc	22	4	4	8	14	2		17	5	14	21	2	24	4	2	2	14	15	3

Sampl	D0902	D0904	D0905	D0907	D0909	D0910	D80914	D0915	D0917	D0920	D0912	D0913	D0909-2	D0914-R	D0918-1	D0918-2	D0922-1	D0922-2	D0924
Cr	40	< 20	< 20	30	< 20	< 20		30	50	50	< 20	30	40	< 20	< 20	< 20	40	< 20	20
Co	22	2	1	7	7	1		16	8	14	7	< 1	21	< 1	1	< 1	15	7	1
Ni	< 20	< 20	< 20	< 20	< 20	< 20		< 20	< 20	20	< 20	< 20	< 20	< 20	< 20	< 20	< 20	< 20	20
Zn	80	< 30	< 30	40	70	30		90	30	50	110	< 30	80	40	40	< 30	50	70	30
Ga	19	12	13	15	21	14		20	18	16	18	13	19	16	19	19	16	23	10
Tl	0.05	0.19	0.52	0.47	0.48	0.46		0.41	0.54	0.21	0.2	0.54	0.1	0.73	0.42	0.49	0.15	0.33	0.41

Table 2

Sample name	Isotope ratios						Age							
	$^{207}Pb/^{235}U$	2σ	$^{206}Pb/^{238}U$	2σ	$^{207}Pb/^{206}Pb$	2σ	$^{235}U-^{207}Pb$	2σ	$^{238}U-^{206}Pb$	2σ	$^{232}Th-^{208}Pb$	2σ	$^{207}Pb-^{206}Pb$	2σ
D0906-2	0.31903	0.01579	0.04262	0.00136	0.054288793	0.002052018	281.2	12.2	269.05	8.41	382	85	269.6	8.43
D0906-6	0.31848	0.01694	0.04207	0.00136	0.054905578	0.002324074	280.7	13	265.65	8.41	407.4	94.7	266.11	8.44
D0906-7	0.30387	0.01797	0.04382	0.00143	0.050288525	0.002482098	269.4	14	276.47	8.83	207	114	275.93	8.77
D0906-8	0.29395	0.01654	0.04170	0.00156	0.051124201	0.002148972	261.7	13	263.36	9.65	245.4	96.8	263.18	9.59
D0906-9	0.30686	0.01691	0.04181	0.00156	0.053230771	0.002156122	271.7	13.1	264.04	9.65	337.6	91.8	264.58	9.66
D0906-10	0.28987	0.01557	0.04305	0.00160	0.04883147	0.001892638	258.5	12.3	271.71	9.89	138.7	91	269.23	9.69
D0906-12	0.29598	0.01560	0.04151	0.00154	0.051715178	0.001932478	263.3	12.2	262.19	9.53	271.8	85.7	262.31	9.49
D0906-14	0.28405	0.01896	0.04240	0.00161	0.048585739	0.002664285	253.9	15	267.69	9.96	127	129	266.31	9.85
D0906-18	0.29943	0.01538	0.04197	0.00156	0.051744941	0.001838237	266	12	265.03	9.65	273.1	81.4	265.15	9.59
D0906-20	0.30614	0.01782	0.04124	0.00155	0.053836313	0.002393685	271.2	13.9	260.51	9.6	363	100	261.02	9.62
D0906-24	0.28327	0.01194	0.04133	0.00109	0.049713351	0.001635493	253.25	9.45	261.07	6.75	180.6	76.7	260.22	6.68
D0906-26	0.31008	0.01448	0.04222	0.00113	0.053261221	0.002040742	274.2	11.2	266.58	6.99	338.9	86.8	266.91	6.99
D0906-27	0.31148	0.01296	0.04199	0.00111	0.053794915	0.001731426	275.3	10	265.16	6.87	361.5	72.6	265.67	6.88
D0906-28	0.28250	0.01675	0.04176	0.00115	0.049061792	0.002574262	252.6	13.3	263.73	7.12	150	123	263.15	7.08
D0914-1	0.27719	0.01192	0.03968	0.00105	0.050659272	0.001719559	248.43	9.48	250.85	6.51	224.3	78.5	250.65	6.48
D0914-5	0.27261	0.01152	0.04005	0.00105	0.049371632	0.001630586	244.78	9.19	253.14	6.51	164.5	77.2	252.28	6.45
D0914-7	0.27792	0.01037	0.03957	0.00072	0.050933554	0.00166242	249.01	8.24	250.17	4.46	236.8	75.3	250.12	4.45
D0914-8	0.28394	0.01004	0.03940	0.00071	0.052260997	0.001592805	253.78	7.94	249.11	4.4	295.8	69.6	249.27	4.4
D0914-9	0.26643	0.00920	0.03870	0.00069	0.049936533	0.001477581	239.84	7.38	244.77	4.28	191	68.8	244.51	4.27
D0914-10	0.30477	0.01106	0.03983	0.00072	0.055494657	0.001744588	270.12	8.61	251.78	4.46	431.2	70.1	251.9	4.48
D0914-14	0.29357	0.01111	0.04023	0.00073	0.052924213	0.00175574	261.37	8.72	254.26	4.52	324.5	75.3	254.42	4.52
D0914-15	0.28971	0.01080	0.03998	0.00072	0.052559257	0.001711483	258.33	8.5	252.71	4.46	308.8	74.1	252.84	4.46
D0914-20	0.31925	0.01595	0.04086	0.00167	0.056665203	0.001623141	281.3	12.3	258.2	10.3	477.5	63.3	258.4	10.6
D0914-22	0.28861	0.01438	0.04032	0.00165	0.051910446	0.001478487	257.5	11.3	254.8	10.2	280.4	65.2	255.4	10.2
D0914-24	0.27784	0.01442	0.03875	0.00159	0.051998939	0.001655886	248.9	11.5	245.08	9.87	284.3	72.8	245.68	9.84
D0914-25	0.28179	0.01524	0.03910	0.00161	0.052264812	0.001834673	252.1	12.1	247.25	9.99	296	80.1	247.84	9.97
D0914-29	0.29948	0.01583	0.03921	0.00161	0.055399705	0.001841826	266	12.4	247.93	9.99	427.4	74.1	248.5	10.1
D0914-33	0.32260	0.01746	0.04028	0.00162	0.058082313	0.002102738	283.9	13.4	254.6	10	531.9	79.3	253.8	10.2
D0914-34	0.28526	0.01626	0.03980	0.00161	0.051988824	0.002093598	254.8	12.8	251.59	9.98	283.9	92.1	251.93	9.95
D0914-35	0.27142	0.01418	0.03887	0.00156	0.050638598	0.001697749	243.8	11.3	245.82	9.68	223.4	77.5	245.46	9.57

Table 3

Sample No.	Age, Ma	$^{176}Yb/^{177}Hf$	$^{176}Lu/^{177}Hf$	$^{176}Hf/^{177}Hf$	2s	$\varepsilon_{Hf}(t)$	T_{DM}	T_{DMC} Lu/Hf=0.015	$(^{176}Hf/^{177}Hf)i$	$^{176}Hf/^{177}Hf(DM)_i$	$f_{Lu/Hf}$	2s
D0914												
7.1	249	0.020205	0.000720	0.282747	0.000020	4.47	711	994	0.282743	0.283070	-0.98	0.6904
8.1	253	0.028939	0.001043	0.282768	0.000020	5.15	687	950	0.282763	0.283071	-0.97	0.6957
10.1	251	0.018934	0.000679	0.282795	0.000020	6.21	642	883	0.282792	0.283070	-0.98	0.7096
11.1	239	0.023660	0.000881	0.282796	0.000026	5.97	644	889	0.282792	0.283078	-0.97	0.9200
24.1	248	0.021468	0.000783	0.282758	0.000023	4.78	695	970	0.282755	0.283074	-0.98	0.7974
25.1	252	0.028522	0.001020	0.282760	0.000023	4.84	697	968	0.282755	0.283073	-0.97	0.8254
29.1	266	0.017429	0.000632	0.282797	0.000023	6.23	639	880	0.282794	0.283072	-0.98	0.7990
31.1	268	0.020348	0.000745	0.282730	0.000022	4.28	734	1020	0.282727	0.283057	-0.98	0.7759
D0906												
1.1	281	0.039100	0.001305	0.282853	0.000025	7.54	570	775	0.282848	0.283091	-0.96	0.8850
6.1	280	0.021466	0.000780	0.282785	0.000023	6.16	658	898	0.282781	0.283059	-0.98	0.7979
7.1	269	0.030064	0.001016	0.282750	0.000024	5.07	711	974	0.282745	0.283053	-0.97	0.8604
9.1	271	0.024690	0.000834	0.282783	0.000024	6.04	662	905	0.282779	0.283060	-0.97	0.8364
10.1	258	0.022115	0.000793	0.282800	0.000022	6.75	637	863	0.282796	0.283057	-0.98	0.7653
11.1	263	0.026817	0.000898	0.282820	0.000023	6.31	611	850	0.282816	0.283095	-0.97	0.8222
13.1	253	0.030760	0.001074	0.282825	0.000025	7.51	607	812	0.282819	0.283059	-0.97	0.8887